Commun Nonlinear Sci Numer Simulat 101 (2021) 105850

Contents lists available at ScienceDirect

Commun Nonlinear Sci Numer Simulat

journal homepage: www.elsevier.com/locate/cnsns

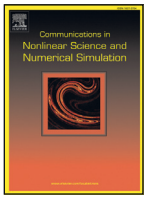

Research paper

Coupled crash mechanics and biomechanics of aircraft structures and passengers

Goong Chen[a,b,*], Jing Yang[c], Alexey Sergeev[a], Mingwei Wang[d], Chunqiu Wei[e], Jean Yeh[f], Philip J. Morris[g], Noah J. Fournier[a], Yining Chen[h], Xingong Cheng[i], Donghui Yang[j], Shuhuang Xiang[k], Marlan O. Scully[b,l]

[a] *Department of Mathematics, Texas A&M University, College Station, TX 77843, USA*
[b] *Institute for Quantum Science and Engineering, Texas A&M University, College Station, TX 77843, USA*
[c] *School of Control and Computer Engineering, North China Electric Power University, Beijing 102206, China*
[d] *COMAC America Corporation, 4350 von Karman Avenue, Newport Beach, CA 92660, USA*
[e] *School of Mathematics, Beijing University of Civil Engineering and Architecture, Beijing 102616, China*
[f] *Department of Mathematics, National Kaohsiung Normal University, Kaohsiung 80201, Taiwan, Republic of China*
[g] *Department of Aerospace Engineering, Pennsylvania State University, University Park, PA 16802, USA*
[h] *School of Electrical and Information Engineering, Tianjin University, Tianjin 300072, China*
[i] *School of Electrical Engineering, University of Jinan, Shangdong 250022, China*
[j] *School of Mathematics and Statistics, and School of Automation, Central South University, Changsha, Hunan 410075, China*
[k] *School of Mathematics and Statistics, Central South University, Changsha, Hunan 410083, China*
[l] *Baylor Research and Innovation Collaborative, Waco, TX 76708, USA*

ARTICLE INFO

Article history:
Received 30 January 2021
Accepted 9 April 2021
Available online 20 April 2021

Keywords:
Aircraft crash mechanics
Passenger biomechanics
Aircraft structural components and fixtures
Injury analysis
LS-DYNA modeling
Supercomputer simulations
Vibration

ABSTRACT

The DYCAST (Dynamic Crash Analysis of Structures) experiments that started at NASA Langley Research Center during the late 1970s have greatly influenced the methodology and thinking of aircraft crashworthiness and survivability studies, and was continued and refined at other aerospace establishments. Nevertheless, so far most of the existing work has emphasized the impact damage to the aircraft section. Issues related to potential passenger injuries have not been properly addressed in the literature, to the best of our knowledge. Here, we study the DYCAST problem integrally by treating and combining impact damage and passenger injuries altogether. We develop the biomechanics by way of modal analysis of passenger dummy motions coupled with the vibration of aircraft structures in order to understand their basic interactions. Two types of mechanical dummies are used in this study. Such a modal analysis can help identify basic injury types, but is valid only in the constructed models, linear regime. However, we are able to extend the linear elastic model to a nonlinear elastoplastic computational model by using the versatile software LS-DYNA as the platform. Computer simulations are carried out on the supercomputer clusters and the numerical results are rendered into video animations for visualization and analysis. One can see, for example, how the passenger-dummy interactive motions with the fuselage and fixtures and the potential injuries caused in the event of general aircraft crashes on a fractal domain.

* Corresponding author at: Department of Mathematics, Texas A&M University, College Station, TX 77843, USA.

https://doi.org/10.1016/j.cnsns.2021.105850
1007-5704/

Nomenclature

$\boldsymbol{\sigma}$	the stress tensor
$\boldsymbol{\varepsilon}$	the linear strain tensor
$\boldsymbol{u}$	the displacement vector
$\boldsymbol{n}$	the unit outward pointing vector
(x, y, z)	spatial coordinates
t	the time variable
$\boldsymbol{\varepsilon}^e$	the elastic part of the strain tensor
$\boldsymbol{\varepsilon}^p$	the plastic part of the strain tensor
ρ	density

1. Introduction

Aircraft crashworthiness and survivability are always top concerns for airplane designers, travelers and transportation regulation agencies. According to some estimates [1], at any given time, there are some 500,000 people in the air flying. Air travel safety has always been rated as the best among all modes of travel because of the long term investments made by the governments of the world and by the time and efforts of numerous researchers on aircraft safety and structural integrity issues.

1.1. Revisiting dynamic crash analysis of structures (DYCAST) and its sequels

Even though there is a long history of aircraft structural safety studies, systematic, integrated research on aircraft structural crashworthiness and integrity modeling and computation did not begin until the work of E.L. Fasanella and his collaborators at the *IDRF* (Impact Dynamics Research Facility) in the NASA Langley Research Center in Hampton, Virginia during the late 1970s [2–4]. The Project was designated *DYCAST* (dynamic crash analysis of structures). At IDRF, a section of a retired Boeing 707 aircraft was dropped to the ground from a control tower about $55 ft$ high, with dummies inside. See Fig. 1. Structural damage was carefully documented, and a finite element model was built to explain the experimentally observed damage. In an early paper by Fasanella, et al. [2], only 300 pieces of finite elements were used.

The work by Fasanella and his collaborators (see [2–4]) established initial benchmarks and has guided the directions of future studies on crash damage modeling and computation for aircraft structures. This work has been continued and refined in academia and the aerospace industry in many countries. We may mention the various more recent papers by researchers

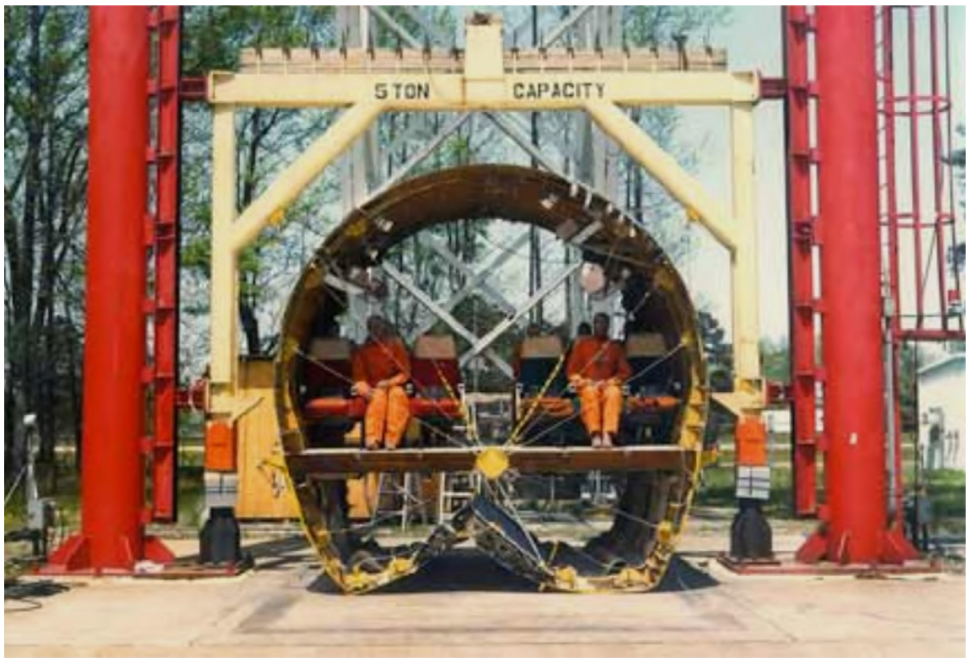

Fig. 1. Drop of a section of a Boeing 707 aircraft to the ground from a height of 55 ft and the visible damage.

in Japan [5–7], China [8,9] and the European Union [10,11], for example. In 2020 Paz et al. [12] proposed enhancement of crashworthiness of commercial aircraft structure by crushable energy absorbers for struts and studied them for a vertical drop scenario. See also the references [13–28] for other designs, optimization and composite materials related to the drop test and crashworthiness studies. The single section of an aircraft in the DYCAST experiment consists of the following components: *fuselage, ring stiffeners, stringers, seats, passengers/dummies, floor, struts, safety belts, overhead cabins*, plus other possible minor items. These components interact with each other through coupling or interface conditions. Thus, there is a great deal of structural complexity in the work of model building. In turn, each component is made of different materials and has varying geometries, yielding diverse dynamic responses in a crash environment. Computationally, there is a large memory requirement in order to achieve the desired accuracy through increasingly fine resolutions. Such computations normally exceed the capacity of a desktop or small workstation and necessarily must be implemented on a supercomputer. These constitute major challenges for the present study.

1.2. Vibration modal analysis of fuselage structure and passenger dummies

In the earlier studies cited in the preceding subsection, the emphasis of the work was on aircraft structural integrity and damage after the crash tests. Little work has been addressed to the study of passenger safety. Passengers' injuries and fatalities can happen due to fires, high-G forces, blunt force trauma and bodily penetration by flying projectiles. The types of injuries suffered by the victims depend on various factors of the air accident, such as the positions of the passengers, whether seat belts were on, the type of collision, the intensity of the impact, etc. As there are so many variables, there are many scenarios. There is obviously a large void to be filled in regarding such a passenger injury study. Yet one thing that is quite certain is that such a study largely depends on the *interactions between the passenger and the aircraft and fixtures.* Here, our treatment does not include the effects of fires.

We study this passenger-aircraft interaction, mathematically speaking, by the method of *vibration modal analysis* of an aircraft fuselage section furnished with passenger dummies. The aircraft section is designed in the same spirit as the *DYCAST* experiment. Such a modal analysis is commonly regarded as *fundamental* in the analysis of most mechanical vibrations. Modal analysis is the determination of natural frequencies and mode shapes of a structure. Usually, damping is neglected as a first step in performing the dynamic analysis. Using the natural frequencies and mode shapes, one can extract characteristic properties of the structural dynamics and understand the response of the system subject to dynamic loading and disturbance. In biomechanics/bioengineering, the use of modal analysis is not new. We mention several representative articles [29–32], see also the references therein, as examples, where the *biomechanics* of human body movements is an important subject originating from the applications in ergonomics, kinesiology, sports medicine, aging, vehicle transport comfort, etc. In addition, in civil and mechanical engineering, a prominent application of modal analysis is the *tuned mass damper* (TMD) [33] that can help damp out vibrations in tall skyscrapers due to wind or seismic effects. TMD application can prevent discomfort, damage, or outright structural failure [33]. In aerospace engineering, for example, in Dimitrijević and Kovačević [34] Dimitrijević and Kovačević performed computational modal analysis on their LASTA aircraft in order to avoid wing flutter in the range of operating speeds of the LASTA. In the automotive industry, passenger safety is a critical design requirement that also depends on car-driver/passenger interactions. Nevertheless, we have not found any work on modal analysis related to automobile car crash tests. Thus, our work here may very well fill in portions of the similar needs for the automotive industry, as the crash conditions being treated here are actually *more general.* Overall, what we are doing may be best termed as developments in *injury and forensic biomechanics*.

1.3. Computer modeling and benchmarking of a ring-stiffened fuselage section

The vibration modal analysis will be carried out *computationally*. To achieve this objective, we need to first build a mathematical and computer model for the ring-stiffened aircraft fuselage section in the DYCAST experiments, calibrate and then validate any computational results against experimental data. Structurally speaking, such a fuselage section is primarily a ring-stiffened aluminum thin-shell structure. However, as it turns out, there is a lack of commonly accepted benchmarks for such ring-stiffened structures with a scale in the range of an aircraft fuselage section, despite a broad online search by the authors. Therefore, computer modeling, validation and benchmarking are a crucial first study for the present paper.

Here, we use the versatile software LS-DYNA [35] as the platform for our structural modeling and design, while the experimental data are chosen from the Japanese work [5,7] as it contains, relatively speaking, the most comprehensive data for our benchmarking purpose. However, the CAD work in Minegishi et al. [5], Kumakura [7] still does not satisfy 100% of our computer modeling needs as some of the seemingly minor design details were omitted in Minegishi et al. [5], Kumakura [7]. Thus, we don't have a model's precise data set to validate against - rather, what we are validating against is the data of an approximate model of a ring-stiffened structure.

1.4. Organization of the paper

The paper is organized as follows; cf. also the flowchart in Fig. 41.

In Section 2, we develop a basic *DYCAST model* by following the design in Minegishi et al. [5], Kumakura [7] as closely as possible, obtaining a ring-stiffened single-section fuselage structure equipped with seats and (passenger) dummies. We

then build the finite element model to compute, analyze and compare predictions against those from [5,7]. Our work here can also be viewed as a benchmark for a ring-stiffened thin shell model for other general purposes.

In Section 3, we first discuss the choices and construction of two types of passenger dummies. The first one is an LS-DYNA dummy [35] while the second is a "make-shift" rubber dummy made due to the limitation of available supercomputer memory storage. We then study their biomechanics by computing and presenting their modal analysis with natural vibration frequencies and mode shapes.

In Section 4, we present the modal analysis of an entire fuselage section containing fuselage, structural supports, seats and passenger dummies. We then again compute and present their modal analysis with natural vibration frequencies and mode shapes, so one can understand the basic types of *structure/dummy interactions*.

The work of modal analysis in Sections 3 and 4 is based on a *linearized elastic model,* as modal analysis can only be performed for linear systems or those in the linear regime. In Section 5, we return to the viscoplasticity model and numerically simulate *general crash tests* for an aircraft section in order to visualize the damage to the aircraft section and the interactive motion of the passenger dummies. The configurations and geometries of general crashes, including a fractal ground and a hill slope, go well beyond the vertical crash test in the literature in order to illustrate and understand the crash mechanisms of structural damages and personnel injuries.

Section 6 provides concluding remarks.

All the mechanical parameters for the various components in this study, such as fuselage, ring stiffeners, stringers, struts, floor, passenger dummies and seats are presented in Appendix A, while the LS-DYNA computer codes are given in Appendix B.

2. Development and construction of a DYCAST fuselage section model, and validation

In this section, we describe the basic mathematical models. The constituent materials under consideration are metal (mainly aluminum) for the fuselage and structural support, rubber for the passenger dummies, concrete for the ground pad, and elastic fabric for the seat belt. All these materials are assumed to be *elastoplastic*, meaning that ([36, p. 135]) below a certain limit load the material is elastic, i.e., the stress tensor is the derivative of the elastic energy function with respect to the strain tensor. When the limit load is reached or exceeded, permanent plastic deformations begin and the stress-strain relation follows a hardening law. Further, the material behavior is rate independent. The limit load is the divide between the linear and nonlinear regimes. We will be considering both linear and nonlinear regimes. The linear regime offers us insights from modal analysis of linear vibrations in Sections 3 and 4, while the nonlinear regime affords us, in Sections 2.2 and 5, the modeling and calculations of fracture, damage and structural collapse. All the computational modeling in this paper is based on the versatile software *LS-DYNA*.

The fundamental equation of motion for continua with N connected subsystems is

$$\rho_i \frac{\partial^2 \boldsymbol{u}_i}{\partial t^2} = \nabla \cdot \boldsymbol{\sigma}_i + \boldsymbol{f}_i, \quad i = 1, 2, \ldots, N, \text{ at } (x, y, z) \in \Omega_i(t), \text{ at time } t, \tag{1}$$

where $\boldsymbol{u}_i = \boldsymbol{u}_i(x, y, z, t) =$ the displacement vector at (x, y, z) at time t of the $i-th$ subsystem; $\rho_i =$ mass density (a constant) of the $i-th$ subsystem; $\boldsymbol{\sigma}_i = \boldsymbol{\sigma}_i(x, y, z, t) =$ the stress tensor at point (x, y, z) at time t of the $i-th$ subsystem; $\boldsymbol{f}_i = \boldsymbol{f}_i(x, y, z, t) =$ body force per unit volume at (x, y, z) at time t; $\Omega_i(t) =$ the spatial domain occupied by subsystem i at time t, $\Omega_i(t)$ may vary with time t. For each subsystem, the boundary condition, on the boundary $\partial\Omega_i(t)$ of $\Omega_i(t)$, is either of the Dirichlet or Neumann type:

$$\boldsymbol{u}_i = \tilde{\boldsymbol{u}}_i \text{ on } \partial\Omega_i(t) \text{ at time } t, \qquad \text{(Dirichlet)} \tag{2}$$

where $\tilde{\boldsymbol{u}}_i = \tilde{\boldsymbol{u}}_i(x, y, z, t)$ is given; or

$$\boldsymbol{\sigma}_i \cdot \boldsymbol{n} = \tilde{\boldsymbol{c}}_i \text{ on } \partial\Omega_i(t) \text{ at time } t, \qquad \text{(Neumann)} \tag{3}$$

where $\tilde{\boldsymbol{c}}_i = \tilde{\boldsymbol{c}}_i(x, y, z, t)$ is given. Between two subsystems *with connection*, there are *interface* or *transmission* conditions across the interface. The interface/transmission conditions across any two components of two subsystems i and $i+1$ are

$$\boldsymbol{u}_i^+ = \boldsymbol{u}_{i+1}^-, \qquad \text{(continuity of displacement)}$$

$$(\boldsymbol{\sigma}_{normal})_i^+ = (\boldsymbol{\sigma}_{normal})_{i+1}^-, \qquad \text{(continuity of normal force),}$$

accross the interface.

There are also the *contact conditions* between the surface of any two subsystems or between a subsystem with itself when contact or impact happens. In our LS-DYNA modeling, the contact conditions for interactions are modeled by the keywords `*CONTACT_ERODING_SINGLE_SURFACE` and `*CONTACT_AUTOMATIC_SURFACE_to_SURFACE` [37, pp. 11-51] with static coefficient of friction (FS), dynamic coefficient of friction (FD), exponential decay coefficient (DC), coefficient for viscous friction (VC) and viscous damping coefficient (VDC) all equal to 0.2.

For interface conditions between two subsystems, see Table 1 in the next subsection.

In our paper, there are a total of 10 types of subsystems (i.e., $N = 10$ in (2.1)); see Fig. 2. However, each subsystem can have *repetitive components*. For example, the ring-stiffeners, stringers, struts, passengers, seats, and seat belts all have

Table 1
Interface modeling between two component systems.

Interfaces	LS-DYNA modeling keywords
fuselage /ring-stiffeners /stringers /struts /floor /seats /rubber passenger dummies /seat belts /ground pad:	*CONTACT_ENRODING_SINGLE_SURFACE
LS-DYNA ATD /seat belt:	*CONTACT_AUTOMATIC_SURFACE_TO_SURFACE
LS-DYNA ATD /seat:	*CONTACT_AUTOMATIC_SURFACE_TO_SURFACE
LS-DYNA ATD /floor:	*CONTACT_AUTOMATIC_SURFACE_TO_SURFACE

Table 2
Description of the lowest 10 modes computed by modal analysis for the LS-DYNA ATD. In the third column ("Mode shape description"), the motions of the ATDs are described in biomedical terms as they could be related to bodily injuries. See the defining terms in Remark 1. In the fourth column ("Mode names"), the motions are described in daily or sports expressions. The reader can click on the corresponding figures to see the computed animations.

No.	*freq.* (Hz)	Mode shape description	Mode names	Videos (click to play)
1	2.6866	Anti-symmetric Lateral Hip Abduction	Seated Slalom Mode	Fig. 11
2	4.3763	Symmetric Sagittal Knee Extension with Hip Flexion	Dolphin Mode	Fig. 12
3	6.053	Anti-symmetric Knee Abduction	Slalom Mode	Fig. 13
4	6.2999	Symmetric Sagittal Body Compression	Greater Inchworm Mode	Fig. 14
5	6.8746	Symmetric Coronal Knee Torsion	Lower Accordion Mode	Fig. 15
6	8.2098	Anti-symmetric Knee Flexion	Bicycle Mode	Fig. 16
7	9.1102	Anti-symmetric Elbow Flexion and Knee Torsion	Running Man Mode	Fig. 17
8	9.4587	Symmetric Shoulder Flexion	Lesser Inchworm Mode	Fig. 18
9	10.99	Symmetric Lateral Shoulder Rotation	Upper Accordion Mode	Fig. 19
10	11.4	Anti-symmetric Lateral Shoulder Rotation and Knee Torsion	Flag Mode	Fig. 20

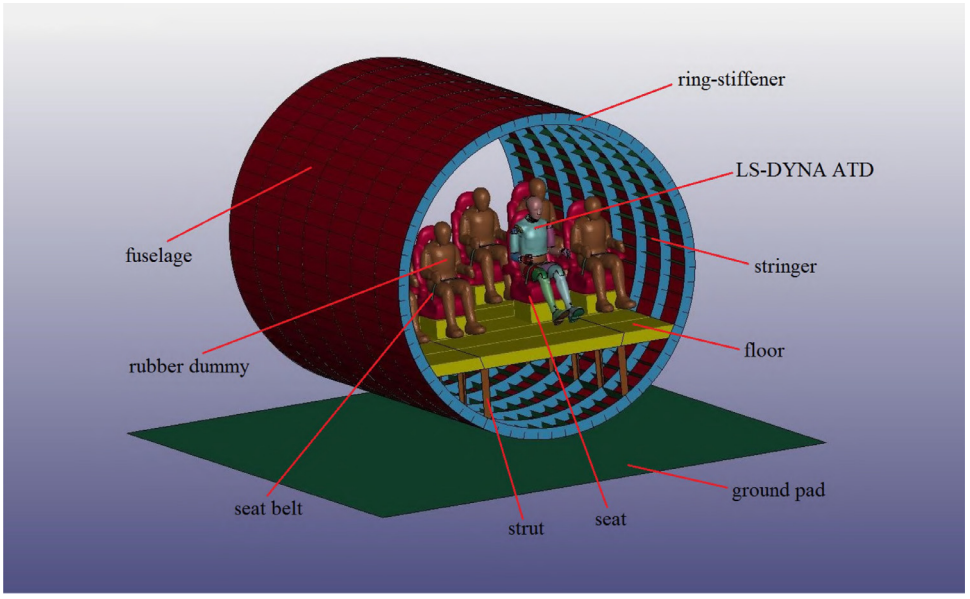

Fig. 2. Configuration of an airliner fuselage section for computer modeling and simulation in this paper. All mechanical parts and passenger dummies marked by component names will be modeled.

multiple numbers and, thus, they can lead to a large number of boundary conditions, interface transmission conditions, and contact conditions.

Continuing from (1) to (3), we define the usual linear strain tensor

$$\boldsymbol{\varepsilon}_i = \frac{1}{2}\left[\nabla \boldsymbol{u}_i + (\nabla \boldsymbol{u}_i)^{\top}\right], \quad \boldsymbol{\varepsilon} = \boldsymbol{\varepsilon}(x, y, z, t), \quad (x, y, z) \in \Omega_i(t), \tag{4}$$

from the displacement $\boldsymbol{u}_i$. In elastoplasticity, this total strain can be decomposed into an elastic part $\boldsymbol{\varepsilon}^e$ and a plastic part $\boldsymbol{\varepsilon}^p$:

$$\boldsymbol{\varepsilon} = \boldsymbol{\varepsilon}^e + \boldsymbol{\varepsilon}^p. \tag{5}$$

When the material is in the (initial) elastic regime, $\boldsymbol{\varepsilon}^p \equiv 0$. Then linear elasticity theory applies, and we have the constitutive relation

$$\boldsymbol{\sigma} = C\boldsymbol{\varepsilon}^e, \tag{6}$$

where C is a 9×9 constant matrix. For an isotropic, homogeneous, elastic solid, from (1), (4) and (6), one can derive the linear elastodynamic equations of motion

$$\rho \frac{\partial^2 \boldsymbol{u}_i}{\partial t^2} = (\lambda + \mu)\nabla(\nabla \cdot \boldsymbol{u}_i) + \mu \nabla^2 \boldsymbol{u}_i + \boldsymbol{f}_i \qquad \text{on } \Omega_i(t), \tag{7}$$

where λ and μ are the usual Lamé constants.

When the material is in the nonlinear plastic regime, the constitutive relation (6) is no longer valid. There is no one-to-one relationship between stress and strain. Rather, the constitutive relation is given in terms of the *rates* of stress and strain. Stress, being dependent on the time history of loading, is only obtainable by integrating the stress rate over time. For the elastoplastic model, we choose the bilinear elastic-plastic model with strain hardening, with or without failure, and with the inclusion of strain rate

$$\frac{\sigma_y}{\sigma_0} = (1 + (\frac{\dot{\varepsilon}}{c})^{1/p}), \quad \text{the Cowper and Symonds model,}$$

where σ_y is the yield stress (value), σ_0 is some reference stress value, and ε is the value of the strain, for some positive constant c. This model, according to our experience, works very well with aluminum alloys.

The (linear) Eq. (7), for $i = 1, 2, \ldots, N$, after finite element discretization in the form

$$\boldsymbol{u}_i \approx \boldsymbol{u}_i^{(h)} = \sum_{k=1}^{n_i^{(h)}} \alpha_{i,k}^{(h)}(t)\phi_{i,k}^{(h)}(x, y, z)$$

and substitution into (7), with all boundary conditions and interface conditions being incorporated using the Garlerkin method, can be assembled into a finite-dimentional ordinary differential equation in the form

$$M\ddot{u}(t) + C\dot{u}(t) + Ku(t) = P(t), \tag{8}$$

where

$u(t) = (\alpha_{1,1}^{(h)}(t), \alpha_{1,2}^{(h)}(t), \ldots, \alpha_{1,N_1}^{(h)}(t), \ldots, \alpha_{i,1}^{(h)}(t), \alpha_{i,2}^{(h)}(t), \ldots, \alpha_{i,N_i}^{(h)}(t), \ldots, \alpha_{N,1}^{(h)}(t), \alpha_{N,2}^{(h)}(t), \ldots, \alpha_{N,n_N}^{(h)}(t))^T$ is a vector-valued function in dimension $n_h \equiv n_1^{(h)} + n_2^{(h)} + \ldots + n_N^{(h)}$; M, C and K are matrices of size $n_h \times n_h$, and $P(t)$ is the forcing function due to gravity body force and other boundary inhomogeneities.

The second order ordinary differential equation system (8) can be solved with initial conditions

$$u(0) = u_0 \in \mathbb{R}^{n_h}, \dot{u}(0) = u_1 \in \mathbb{R}^{n_h}, \tag{9}$$

where u_0 and u_1 are uniquely determined from the initial conditions

$$\boldsymbol{u}(x, y, z, 0) = \boldsymbol{u}_0(x, y, z), \frac{\partial}{\partial t}\boldsymbol{u}(x, y, z, 0) = \boldsymbol{u}_1(x, y, z) \tag{10}$$

where $\boldsymbol{u} = (\boldsymbol{u}_1, \boldsymbol{u}_2, \ldots, \boldsymbol{u}_N)$, and $\boldsymbol{u}_0$ and $\boldsymbol{u}_1$ constitute the two *total* initial conditions for (7) by assembling each component system's two initial conditions for (8): $\boldsymbol{u}_{i,0}$ and $\boldsymbol{u}_{i,1}$, altogether for $i = 1, 2, \ldots, N$. The linear ODE system (8) and (9) collectively has a unique solution $u(t)$, which is a finite element approximate solution to the engineering model in the linear regime.

Now, consider *modal analysis*. Its concept is akin to Fourier series or atomic physics wherein one breaks up the mathematical solution into fundamental units of *eigenfunctions* and/or eigenvectors. Assume that the matrices M, C and K in (8) are all real constant matrices. Then the superposition principle gives

$$u(t) = u_p(t) + \sum_{j=1}^{n_h} c_j w_j(t), \quad c_j \in \mathbb{C} \text{ (field of complex numbers)}, \tag{11}$$

where $u_p(t)$ is a particular solution and $\{w_j(t) | j = 1, 2, \ldots, n_h\}$ is a set of linearly independent nontrivial solutions satisfying the homogeneous equation system

$$M\ddot{w}_j(t) + C\dot{w}_j(t) + Kw_j(t) = 0, \quad j = 1, 2, \ldots, n_h \tag{12}$$

As M, C and K are constant matrices, each nontrivial solution is of the form $e^{\lambda_j t}\boldsymbol{\phi}_j$, satisfying the generalized eigenvalue problem

$$(\lambda_j^2 M + \lambda_j C + K)\boldsymbol{\phi}_j = \boldsymbol{O} \in \mathbb{R}^{n_h}, \tag{13}$$

when the n_h-dimensional vector $\boldsymbol{\phi}_j$ is the only (multiplicity one) vector provided that λ_j is the only root to the algebraic equation

$$\det\left(\lambda^2 M + \lambda C + K\right) \equiv p(\lambda) = 0 \tag{14}$$

If the polynomial $p(\lambda)$ has λ_j as a multiplicity solution, then we look for candidate solutions $w_j(t)$ to (12) in the form

$$t^k e^{\lambda_j t}\boldsymbol{\phi}_{j,k}, \quad k = 0, 1, 2, \mu_j - 1, \text{ where } \mu_j = \text{ multiplicity of } \lambda_j.$$

Because the damping matrix C in (13) is generally nontrivial, the eigenvalue λ_j satisfying (13) may have a nonzero real part

$$\lambda_j = \alpha_j + i\beta_j, \quad \alpha_j, \beta_j \in \mathbb{R} \tag{15}$$

In modal analysis, we are looking for *harmonic motions*, i.e., we want $\alpha_j = 0$ in (15). To this end, we drop C in (12) and consider

$$M\ddot{w}_j(t) + Kw_j(t) = 0, \quad j = 1, 2, \ldots, n_h. \tag{16}$$

Solutions $w_j(t)$ now take the form

$$w_j(t) = e^{i\omega_j t}\boldsymbol{\phi}_j \tag{17}$$

yielding

$$(-\omega_j^2 M + K)\boldsymbol{\phi}_j = 0 \tag{18}$$

The eigenvector $\boldsymbol{\phi}_j$, which has entries that are coefficients corresponding to the finite element basis $\boldsymbol{\phi}_{i,k}^{(h)}$, will provide the *natural mode shapes* in modal analysis.

Even though the equation of motion (1) in solid mechanics is universal, in computational modeling constituent parts are often replaced by asymptotic approximations such as plates and thin shells as they can better reflect the material's physical behaviors and reduce computational cost. For example, the fuselage is almost always modeled as a *thin shell*. Here the ground pad is regarded as a *plate*. As *LS-DYNA* is a commercial software package and not open-source, the users (i.e., us) are only provided some rudimentary knowledge about the model and algorithms according to *LS-DYNA's keywords [37]*. The success of computational modeling by *LS-DYNA* hinges on the selection of the most appropriate keywords for models and computational schemes. Therefore, in our subsequent work, we will clearly specify what keywords are used and also provide the *LS-DYNA* computer codes for the community to share, reproduce and critique.

2.1. The model's mechanical design

In the original *DYCAST* experiment [2,3], a section of the Boeing 707 fuselage with internal furnishings and passenger dummies was used for the vertical drop test. However, the design details were not completely known. More detailed information is available in the work carried out at the National Aerospace Laboratory of Japan in 2001 using a YS-11 airliner fuselage section [7], and at the Structure Drop Test Facility in the Airplane Strength Research Institute, in Xi'an, China [9] in 2015 using a generic, unspecified airliner fuselage section model. In this paper, we will adopt the design configuration similar to the Japanese version in Minegishi et al. [5], Iwasaki et al. [6], Kumakura [7], as shown in Fig. 2.

The mechanical parts and fixtures that will be modeled are the *fuselage, ring-stiffeners, stringers, struts, floor, seats, and seat belts*, while the overhead bin will be omitted. Their material properties are listed in various tables in Appendix A.i. However, we will use two types of passenger dummies that require a more detailed separate treatment. Their material properties are given in Appendix A.ii.

Between each two mechanical components in contact, certain *contact or transmission conditions* must be prescribed. All the pairwise transmission conditions by LS-DYNA models are listed in Table 1:

Note that any two objects at the initial time may not be in contact with each other but later may get into contact, penetration or breakup when the impact between them happens. The differences between the two types of contact conditions are:

(i) `*CONTACT_ENRODING_SINGLE_SURFACE` is commonly used in impact simulations. Eroding contact between mechanical parts/fixtures and rubber dummies is defined so that the contact erodes as the element erodes. This allows the contact to work correctly as layers of the parts erode during penetration. Use of an eroding contact automatically invokes a negative volume failure criterion for all solid elements in the model of rubber dummies. A negative volume failure criterion circumvents an error termination due to negative volume by deleting solid elements that develop negative volume.

(ii) `*CONTACT_AUTOMATIC_SURFACE_TO_SURFACE` is defined for the four components: seat, seat belt, floor, and the LS-DYNA ATD (where ATD means "mannequin dummy"). As LS-DYNA ATD is a complex body coosisting of many small components, it is necessary to define a more detailed and precise contact between the ATD and other parts in order to increase computational efficiency. In crash analysis, this contact type is a recommended contact type since, in crash simulations, the orientation of parts relative to each other cannot always be anticipated as the model undergoes large deformations. As mentioned in LSTC [37], automatic contacts check for penetration on either side of a shell element.

Table 3
This table is the counterpart of Table 2 for the lowest ten modes of the rubber dummy computed by modal analysis.

No.	f (Hz)	Mode shape description	Mode name	Video (click to play)
1	0.55349	Symmetric Coronal Knee Torsion	Lower Accordion Mode	Fig. 21
2	0.56442	Anti-symmetric Sagittal Knee Flexion	Bicycle Mode	Fig. 22
3	0.82319	Symmetric Sagittal Knee Extension with Hip Flexion	Dolphin Mode	Fig. 23
4	0.90621	Anti-symmetric Coronal Knee Abduction	Slalom Mode	Fig. 24
5	1.7697	Symmetric Sagittal Body Compression	Inchworm Mode	Fig. 25
6	1.8941	Symmetric Lateral Shoulder Rotation	Upper Accordion Mode	Fig. 26
7	1.9354	Anti-symmetric Lateral Shoulder Rotation and Knee Torsion	Flag Mode	Fig. 27
8	1.9774	Greater Anti-symmetric Elbow Flexion and Knee Torsion	Greater Running Man Mode	Fig. 28
9	1.9852	Lesser Anti-symmetric Elbow Flexion and Knee Torsion	Lesser Running Man Mode	Fig. 29
10	2.0167	Symmetric Lateral Knee Rotation	Charleston Mode	Fig. 30

Table 4
The sequential orders of mode shapes of ten lowest frequency modes of the rubber dummy are rearrangements of those of the LS-DYNA ATD modes.

LS-DYNA	1	2	3	4	5	6	7	8	9	10
Rubber	N/A	3	4	5	1	2	8,9	5	6	7

Please note that the above conditions in Table 1 serve as *homogenizations and approximations*. It is always a serious challenge to model the effects of rivets as there are many of them between structures and supports. They have been studied in the literature (see, for example, [9,38]). However, modeling each rivet *individually*, even if mathematically workable, is not an option here due to the large memory storage requirement.

2.1.1. Fracture criteria

The elastoplastic model of various materials shows that they will suffer fracture and damage once certain threshholds have been exceeded. There are various criteria for fracture and crack growth. Here, our fracture criteria are based on LS-DYNA [39], and are as follows:

- $p \geq p_{min}$ where p is the pressure (positive in compression), and p_{min} is the pressure at failure.
- $\sigma_1 \geq \sigma'_{max}$, where σ_1 is the maximum principal stress, and σ'_{max} is the principal stress at failure.
- $\sqrt{\frac{3}{2}\sigma'_{ij}\sigma'_{ij}} \geq \bar{\sigma}_{max}$, where σ'_{ij} are the deviatoric stress components, and $\bar{\sigma}_{max}$ max is the equivalent stress at failure.
- $\epsilon_1 \geq \epsilon_{max}$, where ϵ_1 is the maximum principal strain, and ϵ_{max} is the principal strain at failure.
- $\gamma_1 \geq \gamma_{max}$ where γ_1 is the shear strain, and γ_{max} is the shear strain at failure.
- The Tuler-Butcher criterion,

$$\int_0^t [\max(0, \sigma_1 - \sigma_0)]^2 dt \geq K_f,$$

The parameter "Failure strain for eroding elements" (FS) in the card *MAT_PLASTIC_KINEMATIC is set to 0.1. In the card *MAT_ADD_EROSION, the parameter "Volumetric strain at falure" (VOLEPS) is set to 0.1, and "Shear strain at failure" (EPSSH) is set to 0.1. □

2.2. Validation of computational modeling against an experimental drop test by Kumakura, et al. [5]

A section of an aircraft is primarily a *ring-stiffened structure*. These thin-shelled structures are often used in airplane, submarine, pipeline and tunnel constructions, making their use quite widespread.

The study in this paper is computational in nature. For computational mechanics, the work of *validation* is always indispensable and important. In this subsection, we validate our computational structural model to demonstrate the correctness and consistency of our methodologies through comparisons with experiments. However, there are not yet benchmarks in the literature for our purpose, to the best of our knowledge, despite an extensive search for comprehensive sets of experimental data for such ring-stiffened circular thin-shelled structures. As a result, our study can more broadly *provide a benchmark for such structures* within the scale of a few meters in diameter.

What we have found out is that the crash drop test by Kumakura, et al. [5] offers a concrete example and provides the best of such data available, again to the best of our knowledge. The drawback is that their data set is incomplete as far as the specified values of certain system parameters are concerned with regard to a section of the YS-11 aircraft. Nonetheless, it constitutes the best experimental results for our validation study.

Our aircraft section, with passenger dummies, is constructed as shown in Fig. 2, with details of material properties and system parameters as given in Appendix A. Table A.1 lists some key parameters from [5,7]. One notes that several other

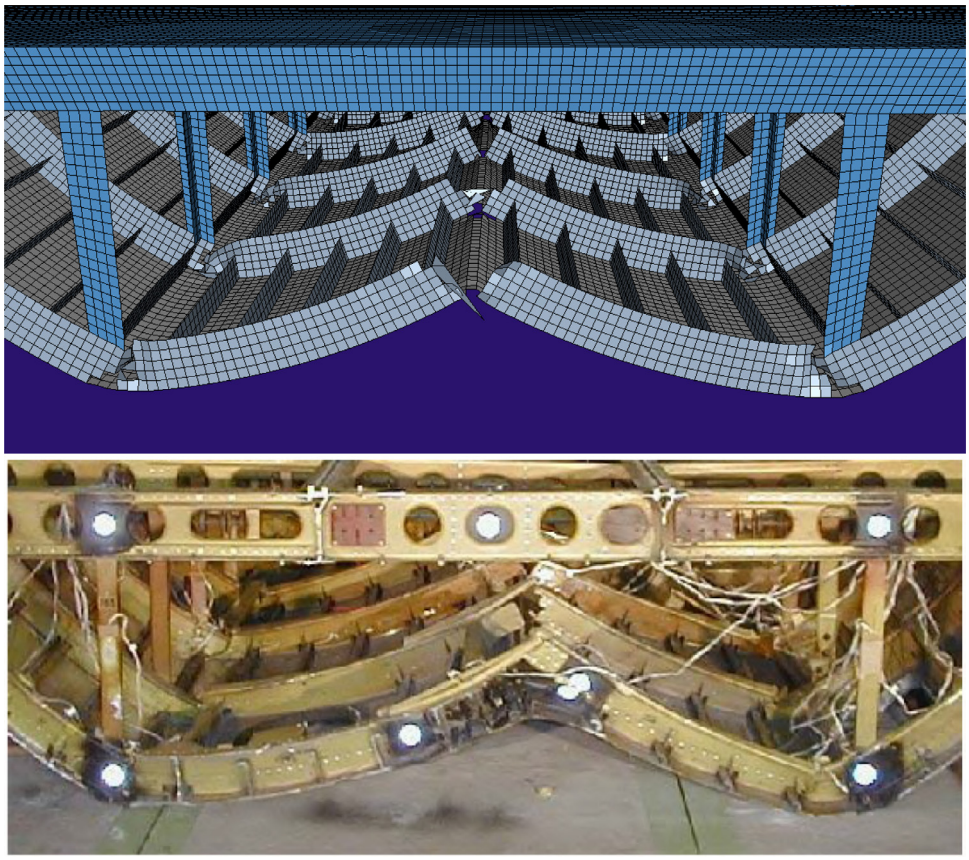

Fig. 3. The upper panel shows the outcome of our simulated drop test, while the lower panel shows the outcome of the drop test experiment by Kumakura, et al. [5].

important parameters, such as fuselage skin thickness, weights of dummies, the width and weight of each set of ring-stiffener, were not given explicitly due to the aforementioned lack of information. Thus, we need to choose certain values that we believe are reasonable. Our chosen values are given in Table A.1.

This aircraft section is dropped from a height of 55 feet, with velocity as indicated in Table A.9, by following [5]. The computational outcome of structural damage/fissure is shown in the upper panel of Fig. 3, which can then be compared with the photo of the real damaged experimental structure in the lower panel. One can observe that the graphics in the two panels are closely consistent. The corresponding animation video from our supercomputer output is viewable by clicking Fig. 10, which contains the front, isometric, side, separate, close and transparent rendering of views that can help understand the drop-test motion more visually.

We now perform vibration data analysis for the drop test. In Fig. 4, part (a), excerpted from [5], one can see the locations of acceleration sensors for the drop test experimental setup on various parts of the fuselage, fixtures and dummies. There were a total of 5 sensors. In our setup, as shown in Fig. 4, part (b), we have also designated 5 places where computational numerical values of vertical acceleration can be extracted. Such acceleration curves contain high frequency components many of which are related to *noise*, as shown in Fig. 5(a). Here we have chosen the same CFC 20 low-pass filter [40] to remove the noise. What we have obtained are curves of acceleration with a low cutoff frequency. These curves are displayed in the same graphics for direct visual comparisons by the reader. One can see that for sensor curves/values on the fuselage, floor, strut and ceiling. (cf. Figs. 5–8, respectively), our values are consistent with those obtained by Kumakura, et al. [5]. With regards to sensor location placed on the dummies' chest, however, our values display some phase differences.

The above curves and corresponding comparisons have provided a validation for our computational modeling vis-a-vis the best experimental data sets available in terms of *vibration characteristics*.

Legends of curves: Throughout Figs. 5–9 in the following, in part (b) of each set of figure, the red curve represents our filtered curve from part (a), overlaid with the black curve representing the experimental curve from [5], and also the broad grey curve representing the computed curve based on the numerical modeling from [5].

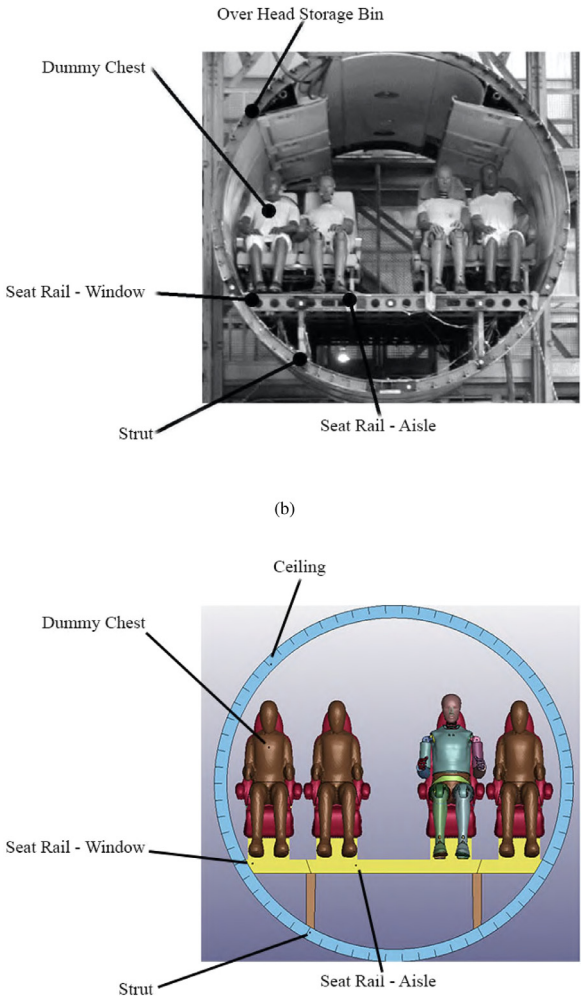

Fig. 4. (a) Locations of sensors in the drop test in Minegishi et al. [5]; (b) Locations of sensors in our computations. There are 5 in total in each (a) and (b).

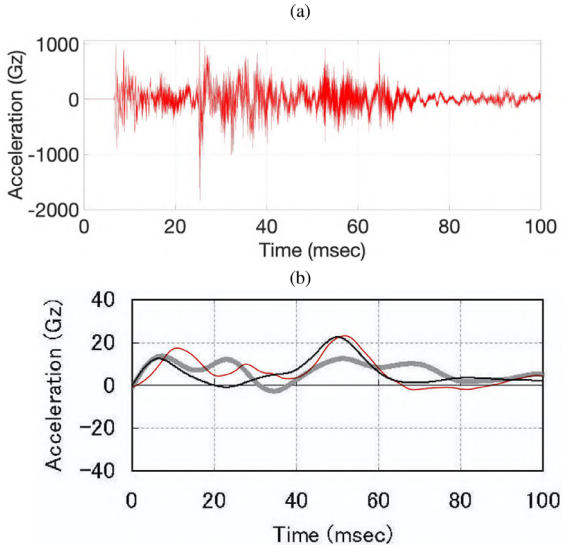

Fig. 5. Vertical acceleration at sensor location "Seat Rail - Window" in Fig. 4, extracted from our simulations; (a) unfiltered curve; (b) comparisons with [5].

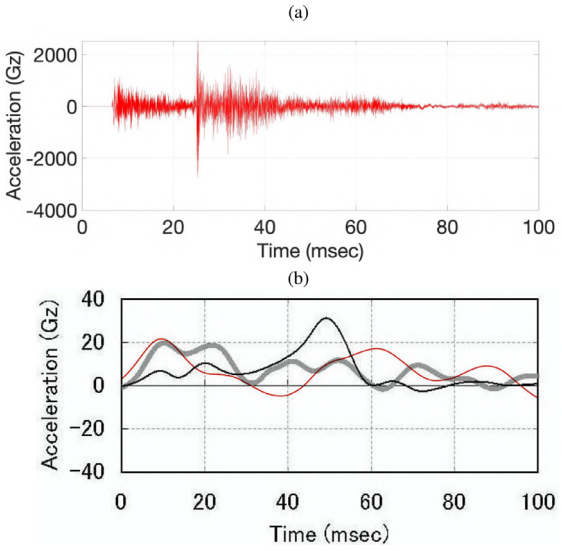

Fig. 6. Vertical acceleration at sensor location "Seat Rail - Aisle" (a) unfiltered curve; (b) comparisons with [5].

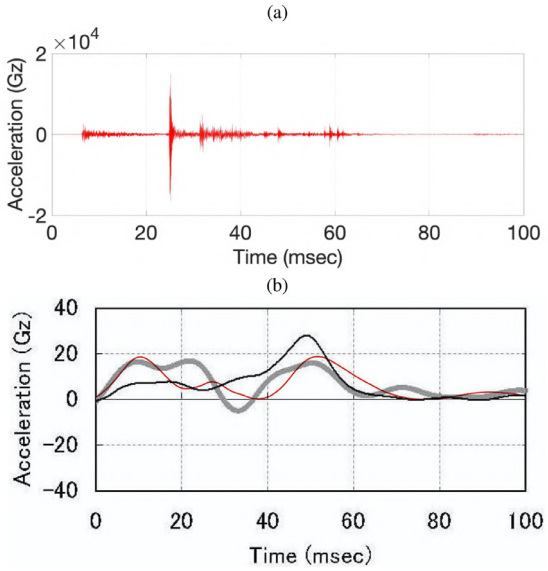

Fig. 7. Vertical acceleration at sensor location "Strut" (a) unfiltered curve; (b) comparisons with [5].

3. Biomechanics: modal analysis of passenger dummies

Crash test dummies, formally named *anthropomorphic test devices (ATDs)*, are mannequins which can be made into various sizes and shapes to fit each individual. ATDs are equipped with sensors that measure forces, moments, displacements, and accelerations, capable of supplying data to indicate the extent of injuries. LS-DYNA has listed, according to [41], 10 dummy models. Out of them, our choice of the LS-DYNA dummy is the one named *"Hybrid III 50th percentile LSTC_NCAC"*, which contains simulated muscle groups and even internal organs. It is chosen mainly because it is one of the newest models.

Even though such a choice of human dummy is convenient to use and supposedly well tested to be canonical, we have found that their use is computationally time-consuming when more than a couple dummies are used. The reason is due to the intricate connected parts in an ATD. Therefore, we have a need to develop a simpler passenger dummy that can be used in larger numbers in supercomputer simulations. This leads to our "make-shift" design of a test dummy by ourselves made of rubber-like material. We call the LS-DYNA dummy an ATD while our own designed dummy is called a *rubber dummy*. Its design is discussed in Section 3.1.

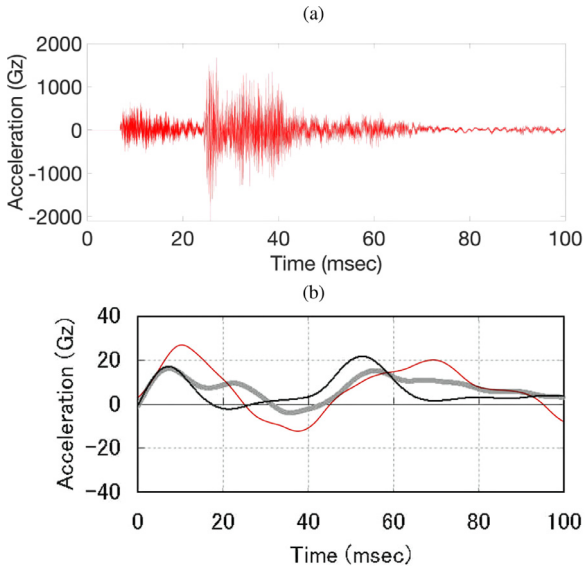

Fig. 8. Vertical acceleration at sensor location "Over Head Storage Bin" (a) unfiltered curve; (b) comparisons with [5].

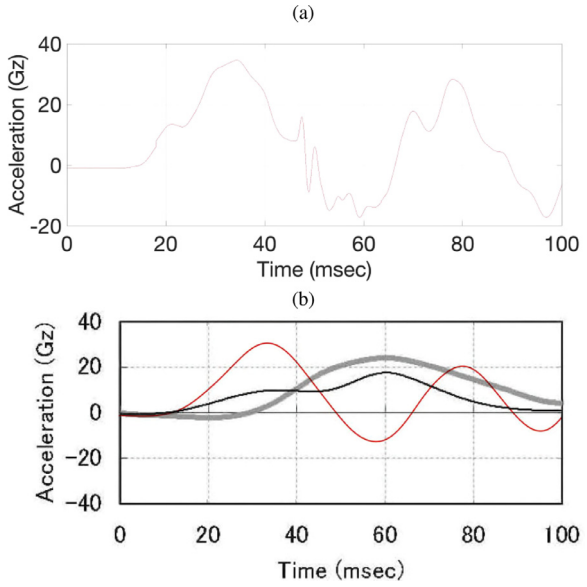

Fig. 9. Vertical acceleration at sensor location "Dummy Chest" (a) unfiltered curve; (b) comparisons with [5].

We study the modal analysis of the motions of passenger dummies in two stages. The first stage is to study the modal shapes of *stand-alone dummies*. In this process, we can also understand why there is a need to construct rubber dummies. In the second stage, we show modal shapes of dummy motions in the aircraft cabin so we can understand how the motions of dummies interact with the aircraft fixture.

3.1. The natural frequencies of vibration and mode shapes of two types of passenger dummies

We first study the modal analysis of an LS-DYNA ATD. The ATD is set in a seated posture, alone and without any peripheral objects, as shown in Fig. 13. Similarly, a rubber dummy is shown in Fig. 21.

A total of 300 modes have been computed for the ATD, the first 100 of which can be found on our website [42]. Here, we only tabulate and exhibit ten of the lowest frequency modes, in Table 2 and Figs. 11–20. Some relevant interpretations are given in Remark 3.1.

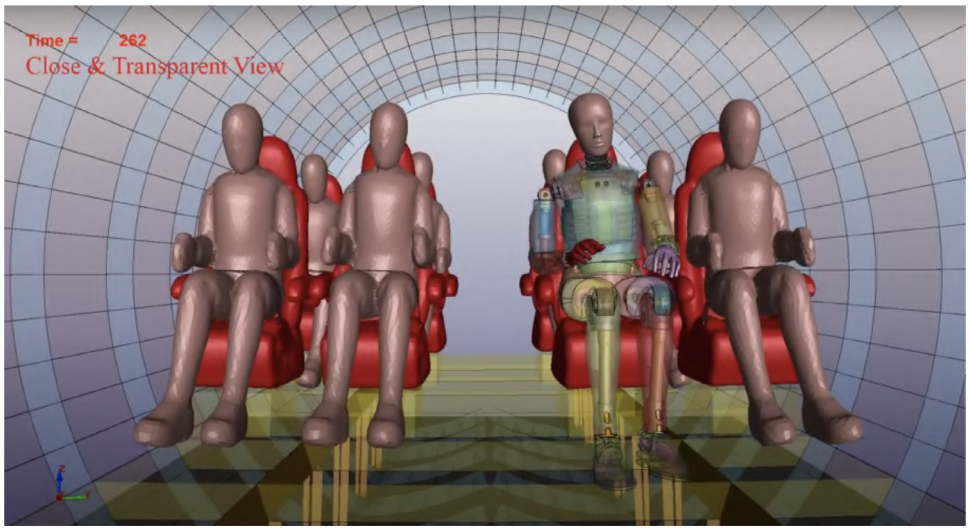

Fig. 10. Visualization of the simulated drop test: a snapshot. For the dynamics, click the graphics.

Fig. 11. Mode 1 - Seated Slalom https://drive.google.com/file/d/1U1u8qOlsY_IDK-H1rX1ejakgTCvqMXoN/view?usp=sharing Click graphics or here to play.

Remark 3.1. In the third column of Table 2, the mode shapes are described with respect to the symmetries of motion as follows:

(1) "Sagittal" refers to body motion confined to the sagittal plane which divides the human body into right and left halves;

(2) "Corona" refers to body motion confined to the coronal plane which divides the front and back of the human body.

In addition, the motion types include compression, torsion, rotation and, furthermore, abduction and flexion, with their meanings as follows:

Abduction: a body motion where a limb moves away from the center of the body while remaining in the coronal plane.

Flexion: a body motion where the angle between two sections of a limb, such as the upper and lower segments of an arm, is decreased and results in a bending action. Flexion is restricted to the sagittal plane.

These remarks also apply to Table 3. □

Fig. 12. Mode 2 - Dolphin https://drive.google.com/file/d/1NHbqW8GwtHpllGLrFpIybxmubIQ342Ax/view?usp=sharing Click graphics or here to play.

Fig. 13. Mode 3 - Slalom https://drive.google.com/file/d/1qCBbxWGCkHbyaCbjHIkhUnT2qiT26LoD/view?usp=sharing Click graphics or here to play.

3.2. Modal analysis of a rubber crash test dummy

Here, we present the vibration modes of a rubber dummy. It is designed according to Appendix A.ii. A total of 100 eigenmodes have been computed, with 40 of them displayed on our website [43]. The first ten eigenmodes are listed in Table 3, with the accompanying mode shapes given in Figs. 21–30, whose motions are viewable by clicking the figures.

3.3. Mode correspondence between LS-DYNA and rubber test dummy

By comparing Figs. 11–20 of the LS-DYNA ATD with Figs. 21–30 of the rubber dummy, one can see that for the ten lowest frequency modes, these two different test dummies vibration mode shapes are essentially of the same types, except that there is a difference in the sequential order of when each mode debuts. This correspondence of sequential orders is indicated in Table 4.

Fig. 14. Mode 4 - Greater Inchworm https://drive.google.com/file/d/1fU_CvqZK65gYGp6gNJMNLR0R2SD1M0IS/view?usp=sharing Click graphics or here to play.

Fig. 15. Mode 5 - Lower Accordion https://drive.google.com/file/d/1ue7VH40TgqxM94v7gXJwnb536H5PnAR3/view?usp=sharing Click graphics or here to play.

This correspondence in Table 4 is obtained by comparisons between the two sets of graphics Figs. 11–20 and 21 fig0022 fig0023 fig0024 fig0025 fig0026 fig0027 fig0028 fig0029–30.

3.4. An artificial dummy by modification of the rubber dummy

Obviously, two types of dummies will behave differently due to their different designs. The differences are reflected in their modal patterns. Nevertheless, their qualitative shapes of motions are fundamentally related. An *essential difference, however, lies in the frequencies.* Fig. 31 shows a plot of the difference between the frequencies of harmonic vibrations of these two types of modes. The frequency band of the rubber dummy lies well below that of the LS-DYNA ATD because *the rubber dummy is much more flexible and, therefore, much more prone to vibrations.* But here, one may ask a natural question: *why can't we use just the well tested LS-DYNA ATD instead of having to consider a rubber dummy?*

Fig. 16. Mode 6 - Bicycle https://drive.google.com/file/d/1dT21nG6g4HAPnsPRKE97y8q1SBc3QP1b/view?usp=sharing Click graphics or here to play.

Fig. 17. Mode 7 - Running Man https://drive.google.com/file/d/19Vq2jb2ZpFYCdDLQJrUfBH6kkNfOcD7p/view?usp=sharing Click graphics or here to play.

Table 5
Computational complexity comparison between an LS-DYNA ATD and rubber dummy.

Dummy	Number of elements	CPU times (s)	Physical times (ms)	Number of CPUs
LS-DYNA	465,951	20,698	49	80
Rubber	78,930	20,698	700	80

The reason is the *computational complexity* involved for the LS-DYNA ATD. As our main objective in the future is to be able to simulate a crash test for a full-scale airliner, where there would be 100 or more passenger dummies in place, the required CPU time and cost would be far too expensive if one uses 100 LS-DYNA ATDs. Consider just a fuselage section with, respectively, one LS-DYNA ATD and one rubber dummy, as shown in the two panels of Fig. 32. The following Table 5 shows the number of needed finite elements involved for the two dummies. The ratio between such numbers (465,951 vs. 78,130) is 5.903, roughly 6 times. These dummies are coupled to the motion of the aircraft section, and when 80 supercomputer processor cores are used to simulate the drop crash test, the slowdown due to the complexity of design for LS-DYNA ATD is

Fig. 18. Mode 8 - Lesser Inchworm https://drive.google.com/file/d/1aqNbHcgNLr-yobrqA9lP7sd_PSscorKM/view?usp=sharing Click graphics or here to play.

Fig. 19. Mode 9 - Upper Accordion https://drive.google.com/file/d/1lXZ7bnI-2m-lKo6Ova0knSDwxZOoESdB/view?usp=sharing Click graphics or here to play.

about 14 times (49 ms vs. 700 ms). Therefore, it would be highly impractical or cost prohibitive to use the LS-DYNA ATDs for large-scale aircraft passenger safety simulations where usually there are over 100 passengers in the cabin. It is for this reason that the design of a computationally inexpensive dummy is called for.

Note that in Table 5, 80 cores of supercomputer processors have been used on the ADA Supercomputer at Texas A&M University's High Performance Research Computing Center.

As noted, the flexibility and excitability of the rubber dummy is excessive. We now rectify this by increasing the *rigidity parameter* of the rubber dummy, leaving all other material properties unchanged, as shown in Table A.11. This new rigidity parameter is *fifty times* of that for the original rubber dummy. This value of rigidity, in Fig. A.13, is chosen by numerical tuning and experimenting through several rounds of supercomputer runs. It is unclear to us, however, if any realistic material could be manufactured to satisfy the properties as listed in Table A.11. Thus, at least presently, such a material must be regarded as *"artificial"*.

With this new material, the ranges of the (most prominent) ten computed frequencies between the rubber dummies and the LS-DYNA ATD have become much more compatible; see Fig. 33(b). However, beyond the range of the most prominent

Fig. 20. Mode 10 - Flag https://drive.google.com/file/d/1kTG12Ar96ZjhagtfQIYsxpzb_PXdlKor/view?usp=sharing Click graphics or here to play.

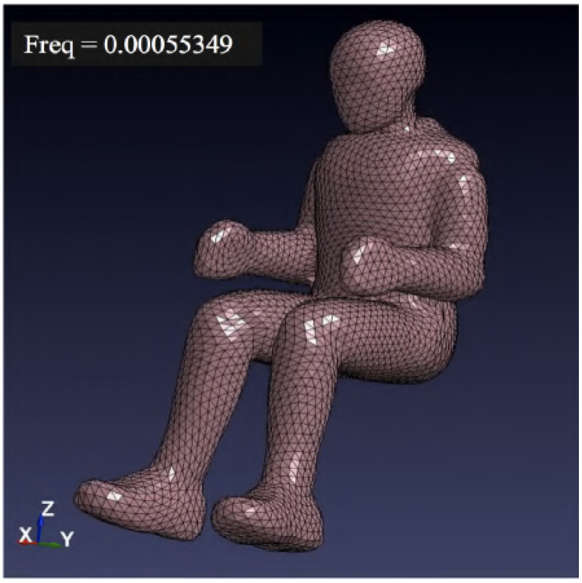

Fig. 21. Mode 1 - Lower Accordion https://drive.google.com/file/d/13STQ-qs8wS5vnHn8xux8_wRlHLbFVTqO/view?usp=sharing Click graphics or here to play.

dozen or so modes, the frequency distribution of the new rubber dummy still lies above that of the LS-DYNA ATD, as shown in Fig. 33(a). This is a deficiency that needs to be rectified in the future.

For our aircraft section crash tests in the next few sections, we will set up the passenger seating by choosing just one LS-DYNA ATD, and one rubber dummy, so one can understand the motions of both types of test dummies, make comparisons, and save a significant amount of computing time.

4. Modal analysis of the natural vibration motion of the test fuselage section

After obtaining the fundamental modes of free vibration of the dummies in the preceding section, we now study the modes of vibration of an entire section of the aircraft, including the fuselage, fixtures and dummies. The primary objective is to see *how the dummies interact with the aircraft structures and its fixtures.*

Fig. 22. Mode 2 - Bicycle https://drive.google.com/file/d/1vlfzcRf-hh7r_4MAyfiBR6Tmrg0nSGT9/view?usp=sharing Click graphics or here to play.

Fig. 23. Mode 3 - Dolphin https://drive.google.com/file/d/1ZrDKcYMsRX85UyCFrX07S_lcA7uR7GPD/view?usp=sharing Click graphics or here to play.

4.1. Total and interactive mode shapes

The computational process is similar to that in Section 3 for the cases of a single dummy according to (1)–(18) in Section 2, whereas we put *all 9 components altogether* and treat the overall system *in the linear regime.* Note that here we are using a total of eight dummies: one is an LS-DYNA ATD and seven are rubber dummies. A total of 400 eigenmodes have been computed.

It is to be expected that some of the components (namely, seat belts, seats, dummies, fuselage, ...) of the overall coupled partial differential equation system may vibrate on their own with rather little coupled motion with other parts of the system. Indeed, the *seat belts* as a component, due to their light weight and highly elastic nature, are much more prone to vibrations than the other parts of the airplane. We have found that the first 244 modes are exactly the vibration modes of the seat belts, showing *negligible coupling motion* with their contacted parts. Fig. 34 and its video animation provide an example. Such modes can be viewed as *trivial modes*. They have little relevance to overall modal analysis and are excluded by us from any further discussions hereinafter. In the rest of this section, our attention will be focused on the nontriv-

Fig. 24. Mode 4 - Slalom https://drive.google.com/file/d/1t9xtLcUOsOAbtN4MH8b7rTyhiZhA5gC8/view?usp=sharing Click graphics or here to play.

Fig. 25. Mode 5 - Inchworm https://drive.google.com/file/d/1ss0N1C2waOKT-E0imvZdN9z57NEsWo8O/view?usp=sharing Click graphics or here to play.

ial modes, especially those exhibiting interactions between the dummies and their environments. There are 80 nontrivial modes, ranging between mode numbers 245 and 398, displayed on our website [45].

4.2. Medical analysis of crash test dummies

Now consider the various injuries that could arise, connecting the dummy motions observed in the free vibration modes (Section 3) to those seen when in interaction with the fixtures of the airplane, noting new areas for concern, as well as those which no longer present possible injury.

While viewing the graphics/snapshots and animation videos showing the motions of the dummies, recall that these motions observed represent *linear vibrations* and their amplitudes are restricted to be small. As far as discomfort or injuries are concerned, such small-amplitude motions may cause a light sprain of muscles at the worst. In the realities of an actual crash, such motions are bound to be intensified and, thus, the motions will be exaggerated (i.e., having larger amplitudes),

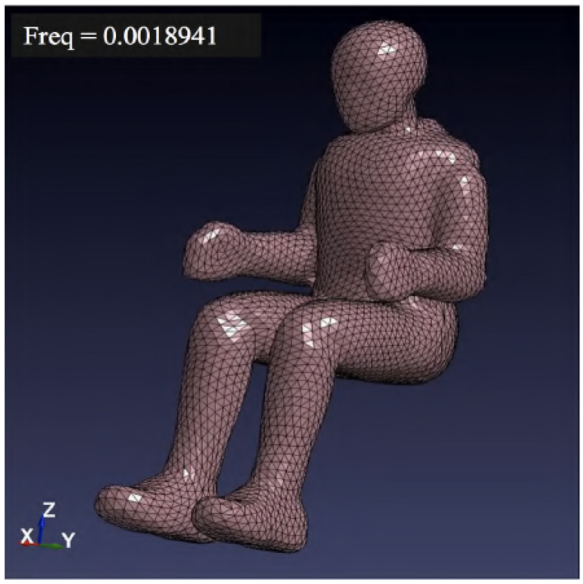

Fig. 26. Mode 6 - Upper Accordion https://drive.google.com/file/d/1lDNk0BBDMNlIrYTRtUV54C7hfSC8MtlS/view?usp=sharing Click graphics or here to play.

Fig. 27. Mode 7 - Flag https://drive.google.com/file/d/18uQ707pPt8wjNCyNnvxNzltl9N0GZMuq/view?usp=sharing Click graphics or here to play.

likely causing real injuries. Our work here will be able to predict which parts of the body will be put under stress in a given motion.

4.2.1. Analysis of primary modes

First, we revisit the graphics and animations as given in Figs. 11–30 in the preceding section. Through visualization and close examining those motions, in Table 6 we have identified and associated them with several basic risk areas and potential injuries according to the websites of the Harris Federal Employee Law Firm [46] and the Mayo Clinic [47], as given in Table 6 below,

4.2.2. Analysis of modes in the fuselage

We first note that there are “tiny” vibrations on the seat belt of the dummy, as shown in Fig. 34. There is no motion on any other parts of the aircraft section. So we exclude such modes related to the seat belt only, and perform only a modal analysis of the fuselage section. There are quite a few modes to consider: Modes 245 - 398. Only a few representative

Fig. 28. Mode 8 - Greater Running Man https://drive.google.com/file/d/1VhGFoI2PraH8RbgPclMmAEhAIO5EQsyO/view?usp=sharing Click graphics or here to play.

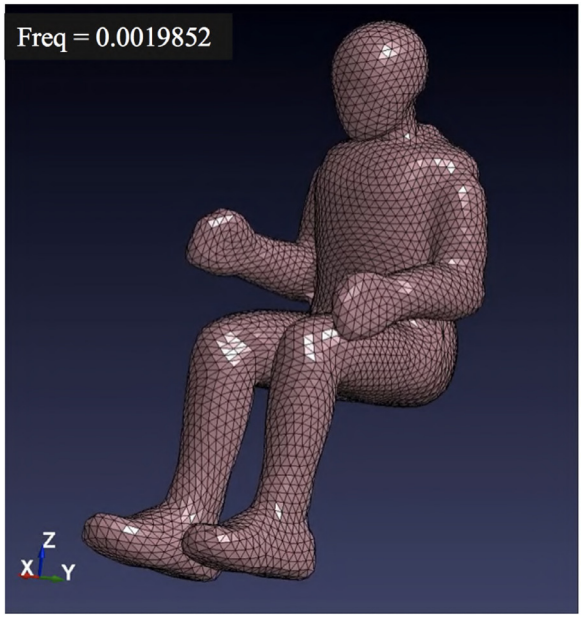

Fig. 29. Mode 9 - Lesser Running Man https://drive.google.com/file/d/1sBkNUl5iJlmJWMNvFSBQzkssyWEvQoxs/view?usp=sharing Click graphics or here to play.

modes are discussed here. We first note that the major areas of concern that are not present in the free vibration modes (cf. Section 4.2.1) correspond mainly to *interactions between the seat back, seat belt, and the dummies*. Three representative examples are described here:

(i) Mode 246: Whiplash

Many of such modes are similar in form to Mode 246, as shown in Fig. 35. At high amplitudes, damage could be done to the head and neck of the passenger as a result of this *whiplash*.

(ii) Mode 266: Head, neck and back trauma

This lateral motion of the head, as shown in Fig. 36 and the associated video, could likely result in injuries in the neck, with severity depending on the intensity of the motion. Mode 266 is one example of a realistic and common mode shape found in an airliner, especially while passing through turbulence, and as a result many passengers experience an aching in

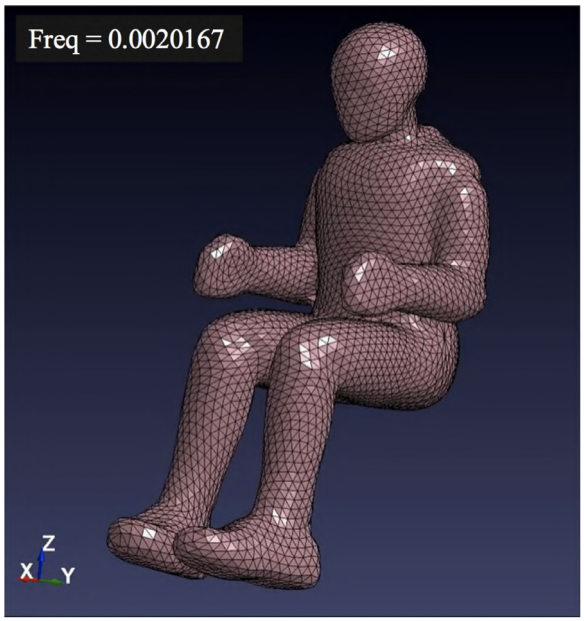

Fig. 30. Mode 10 - Charleston (The Charleston dance was a type of dance that was common in the 1920's, and exhibits motion much like that of the dummy. See [44] for a short video of the dance moves.) https://drive.google.com/file/d/1IwHBZ8e_B2P7Yxis0RdEIoDGD3La0LN8/view?usp=sharing Click graphics or here to play.

Table 6
Potential injuries arising from the fundamental modes of vibration of the rubber and LS-DYNA dummies.

Rubber mode no.	LS-DYNA mode no.	Risk areas	Possible injuries
1	5	Knee	Knee Sprain, Collateral Ligament Tear
2	6	Heel	Bone Fracture
3	2	Head	Concussion
4	3	Knee, Lower legs	Knee Sprain, Collateral Ligament Tear
5	4	Head, Neck, Back	Whiplash, Spinal Compression
6	9	Shoulder	Shoulder Sprain
7	10	Shoulder	Shoulder Sprain
8	7	Neck, Knee	Vertebral Fracture, Knee Sprain
9	7	Neck, Knee	Vertebral Fracture, Knee Sprain
10	N/a	Knee	Knee Sprain, Torn Meniscus

the side of their neck following a flight. Another area that could be affected by this and other similar modes is the back, as this lateral neck motion is often connected to a corresponding tension in the spine. This motion of the back was not previously observed in the free natural modes of Section 3, as it is a result of the seat belt. The seat belt keeps the hips of the dummy in one place, and so rather than getting a motion such as that of Mode 4 of the rubber dummy where the whole body is in motion, all movement occurs in the upper body and puts a more severe tension on the back. We would like to emphasize that this is not to say that airlines should do away with seat belts. The motion described here is only a small negative result that is outweighed by the many advantages of such belts in a passenger aircraft. For example, without a seat belt, Mode 277 would put significant pressure on the back and in severe scenarios result in the passenger leaving their seat. However, the belt keeps the dummy (and passenger) in its seat, reducing the stress put on the passengers back and possible injuries in the spine that could result from a jarring return to their seat.

(iii) Mode 292: Injuries to multiple body parts

One of the most dangerous total modes that we observed was Mode 292 as shown in Fig. 37, as the head, neck, spine, and lower legs were all involved in the motion. One important observation is the motion of the floor in this mode, which shows that this mode involves the coupling of the dummy and the fuselage itself, rather than the dummy and the seat. Physically, this could imply that this mode is only realizable when it is in conjunction with motion of the fuselage, such as is experienced during turbulence. This intense motion could further be prevented by a tighter seat belt, as some space could be noticed between the dummy and the belt. However, no additional simulations were run to test this hypothesis.

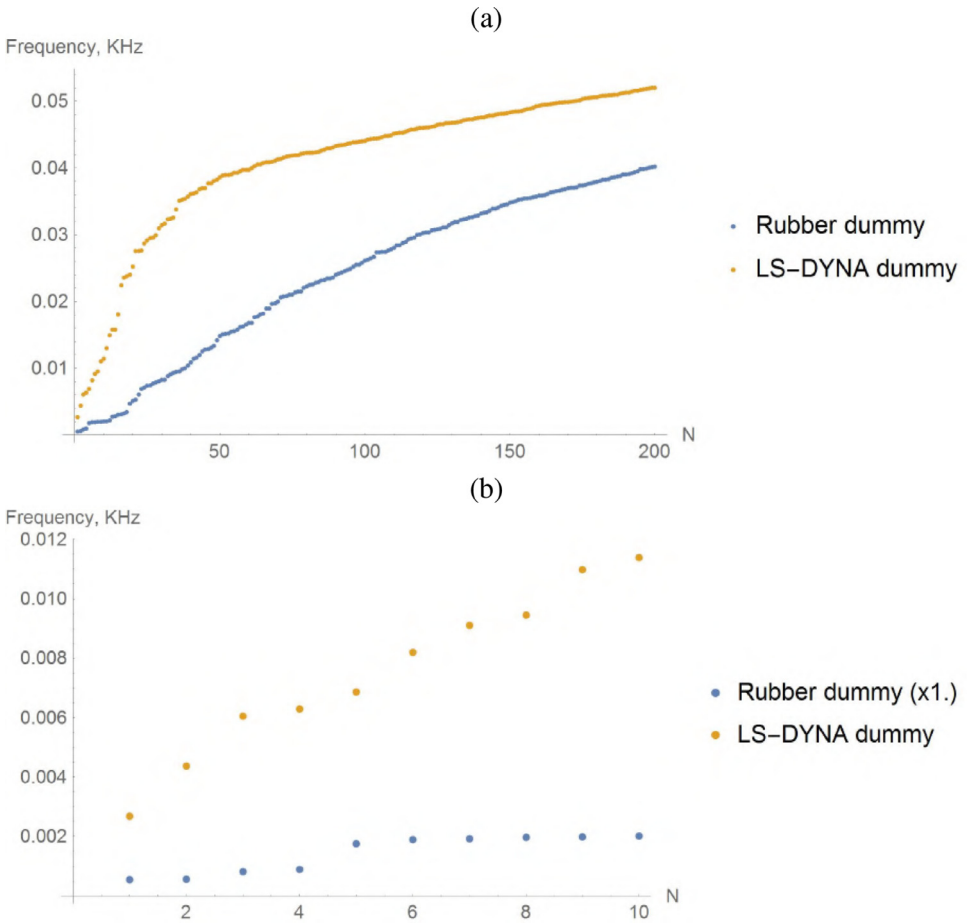

Fig. 31. (a) The difference in frequency distributions between the vibrations of the modes of the LS-DYNA ATD and rubber dummies; (b) Zoomed-in view of the left part of (a).

5. Numerical simulations of general crash configurations with inspections of damage

The greatest power of computational mechanics lies in its *predictive* capability. Once the methodology is validated against suitable benchmarks, one can then apply it to much more general situations. In the preceding sections, we have dealt with only vertical drop tests. Here, we simulate crashes under much more general operating conditions, environments and geometries. Three cases will be considered in the following subsections. Their associated injury risks will be assessed in the fourth subsection.

5.1. Impacting the ground with a roll angle

Here, we consider dropping a fuselage section with a large roll angle. By definition, the roll angle corresponds to rotation with respect to the longitudinal axis which points out of the nose of the aircraft. In our case, the roll angle was set to 135° with respect to the horizontal axis. The calculations show completely different structural damage in comparison with the untilted, vertical drop case.

5.2. Impact on a fractal ground

The appearance of natural terrain could be mimicked on a computer with a *fractal landscape*, see [48]. To produce the fractal landscape, we use a freely available mesh editing software MeshLab. We start from the flat surface of the grounding pad that was used in our previous simulations. A fractal terrain perturbation was generated by *Fractal Displacement* filter using the algorithm “Ridged multifractal terrain”. A detailed algorithm description can be found in a book edited by Ebert [49] (Table 7).

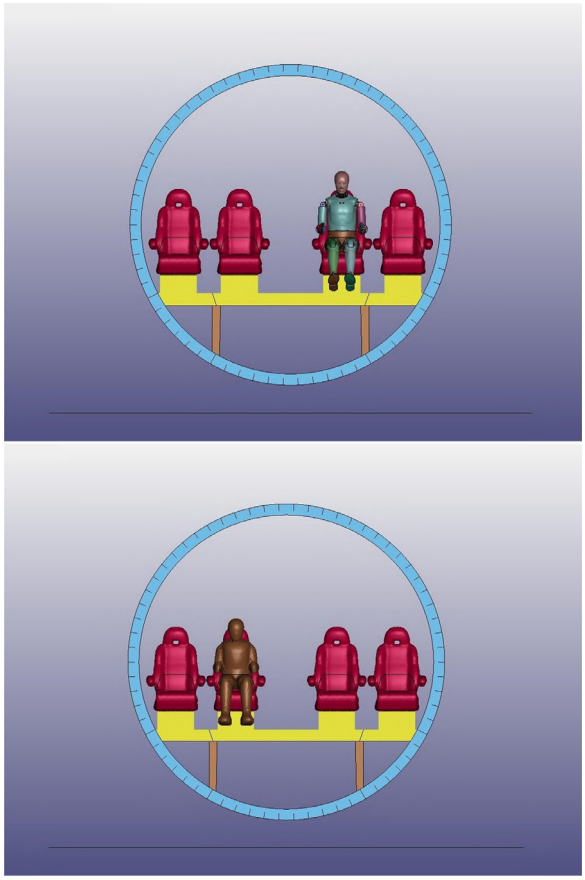

Fig. 32. (a) A single LS-DYNA dummy seated in a fuselage section for a drop crash test; (b) change of seat, with a rubber dummy.

Table 7
Parameters of the *Fractal Displacement* filter in MeshLab. Asterisk marks the parameters changed from their default values.

Property	Value
Max height	4.0%
Scale factor	1
Normal smoothing steps	5
Seed	2
Algorithm	Ridged multifractal terrain
Octaves	8
Lacunarity	4
Fractal increment	0.2
Offset*	0.75
Gain	2.5

The vertical velocity is the same at 15 m/s. We increased the velocity because natural terrain is softer than the solid flat ground. Calculations were performed up to maximal time 0.5 s, with an output interval of 1ms, on 84 processors, with double precision. The calculation time is approximately 53 h. See Fig. 39 and the associated video animation.

5.3. High(er) speed impact of a slope and ground

The geometry and fuselage configuration is as shown in Fig. 40. We allow the fuselage section to drop vertically downward on the slope at a speed of 150 m/s (which is ten times faster than the earlier vertical drop test impact speed of 15 m/s. The choice of even higher impact speed than 150 m/s is possible, but more numerical instabilities begin to emerge.)

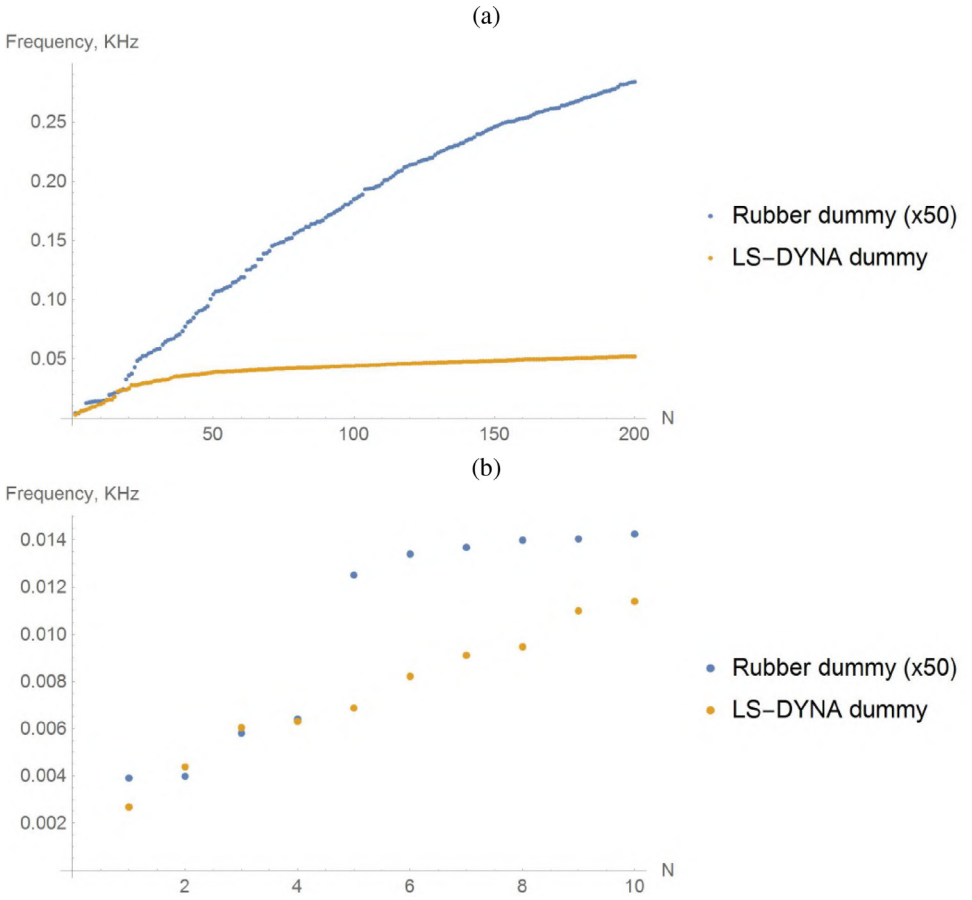

Fig. 33. (a) The distributions of the LS-DYNA modes and the newly designed rubber dummy; (b) zoomed-in view for the first ten modes.

The terrain consists of two planar regions: one flat and one sloped. Fig. 40 contains four snapshots of front, side, bottom and transparent views, respectively. At the impact speed of 150 m/s, we can see that the crash consequences are *gruesome*. Video animations show the following:

(i) severe fragmentation of the impact contact surface of fuselage;
(ii) total collapse of the internal supporting structures, namely, the ring-stiffeners, stringers, struts and floor of aircraft;
(iii) passenger dummies suffer grave bodily injuries, including decapitation and other cranial injuries, amputations of limbs, injuries of the internal organs, and breakup of torso.
(iv) body parts and mechanical fragments fly about and are strewn. Some parts can scatter over a distance of 50 m.

5.4. An overall assessment of injuries

There are many different scenarios that can occur during a crash. We have covered only a small number of cases in this paper. What can be seen and said are the following:

(1) In the classical drop test case where the aircraft section does not have a roll angle, which is shown in Fig. 10 and the accompanying videos, several dummy reactions can be observed. The initial jerk caused by the contact with the ground leads to an initial response of the dummies to tilt forward. In the LS-DYNA ATD, which has mobility in the hips, we can see a bending of the hips that causes the torso to come near to its knees. Depending on the strength of the passenger, this can cause major damage to the back and neck, with a motion similar to that of whiplash. In addition, if the torso comes into contact with the knees, which can be observed in tests with higher drop velocities and a lower stiffness constant for the Rubber Dummy as seen in Fig. 39, further injury can be experienced in the chest area.
(2) In the case of a drop crash onto a natural even terrain, we can note that the difference caused by the fractal terrain is the increase in the angle at which the LS-DYNA ATD bends forward; cf. the video accompanying Fig. 39. The fractal terrain also imparts an increased jerk upon impact, which is manifested in an increased response by the ATD. This can result in a more intense injury of the passengers, however the increase is not large.

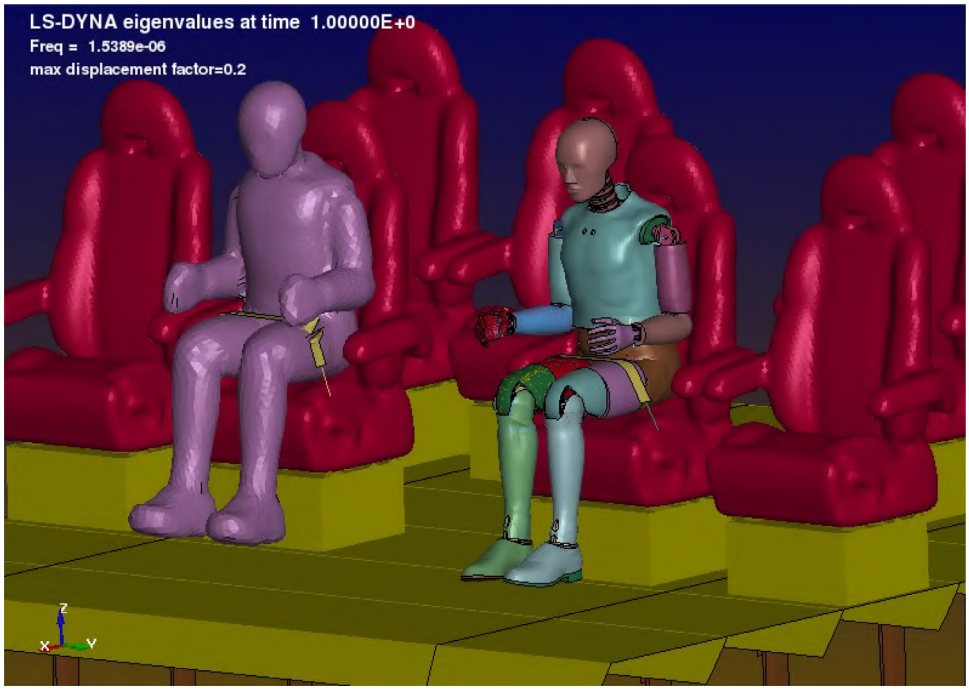

Fig. 34. This is mode 100, which represents a trivial vibration mode of the seat belt. http://www.asergeev.com/files/lsdyna/movies/2020-06-25/03/index.htm Click graphics or here to play.

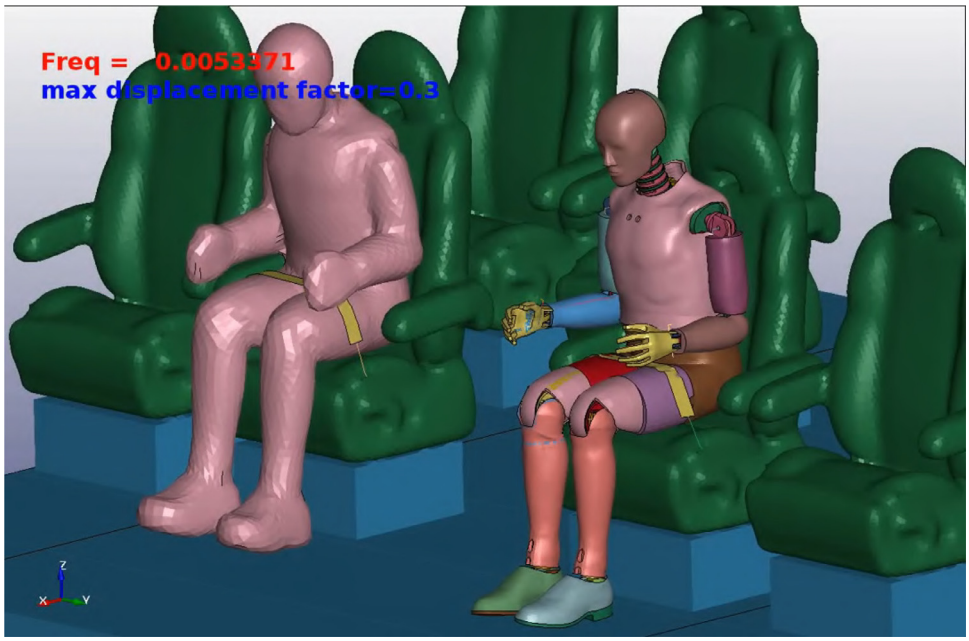

Fig. 35. Mode 246: This shows potential injury of whiplash. https://drive.google.com/file/d/1YHGRA2nyp7Hl5vVaR37yFpLm0FAoE2__/view?usp=sharing Click graphics or here to play.

(3) In the case when there is a large roll angle (say 135 degree as chosen by us), we see that the fuselage experiences a collapse of the ring stiffeners as there is a lack of the struts to absorb the impact force. An overall increase in damage caused is very visible in Fig. 38. As a result, the dummies on the lower side of the fuselage (i.e., nearest to the ground) are subject to major trauma. These dummies come into contact with the side of the fuselage or window at high speeds, leading to severe head trauma. Dummies on the higher side of the fuselage do not experience as great a trauma. However,

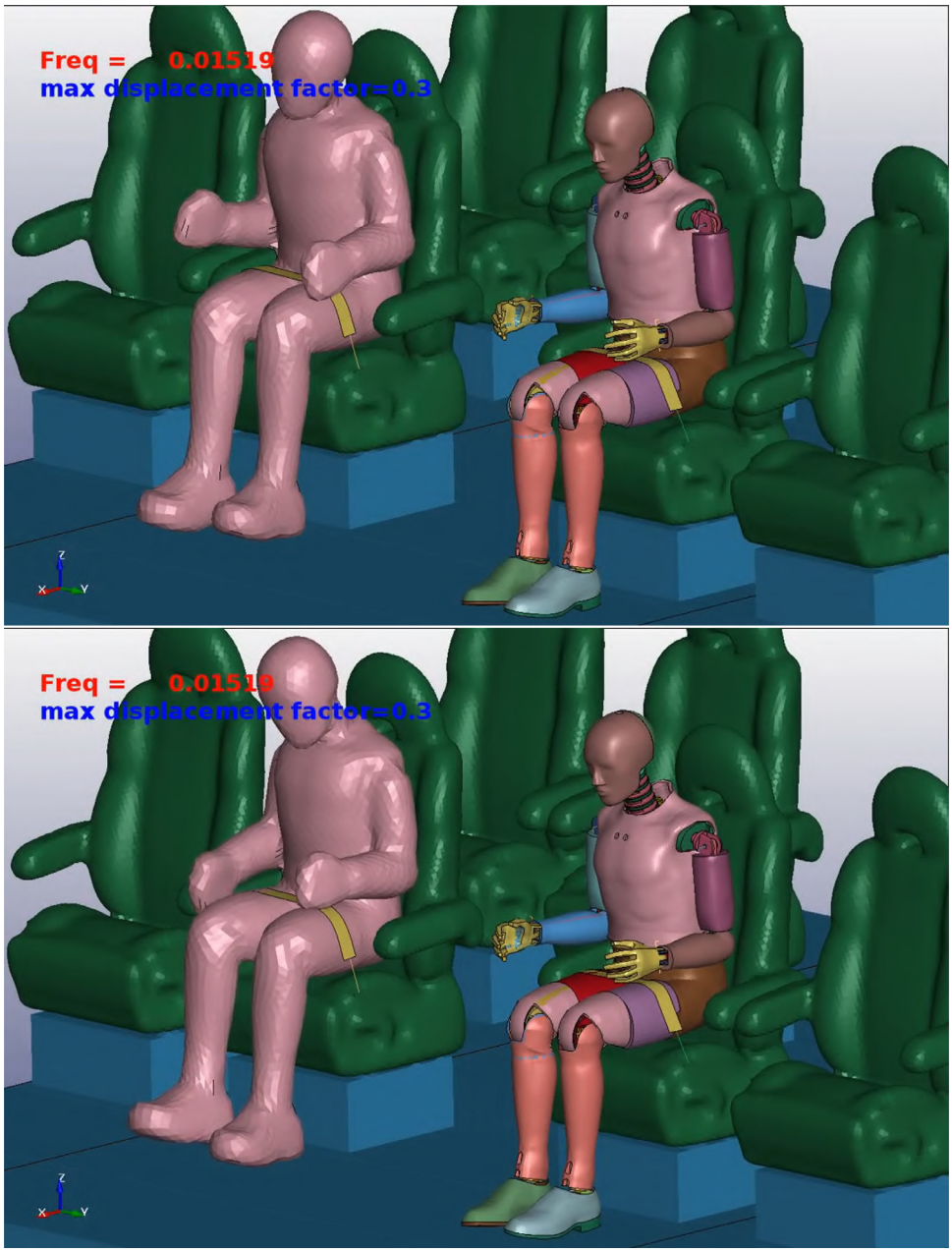

Fig. 36. Mode 266: This mode shows possible head, neck and back trauma. https://drive.google.com/file/d/1J23dsXTbyTn6FZt6Yqe-vqNpCwxAgmOh/view?usp=sharing Click graphics or here to play.

they are still at risk of of injuries to the back and neck caused by the elongation of the spine caused by restraining effect of the seat belt following the initial impact.

It is necessary to note here that although the seat belt can lead to some injuries of the dummies on the higher side, they prevent fatalities stemming from passengers flying off seats and coming into contact with the ceiling upon impact, which would have resulted had the dummies not been fastened in their seat belts. Considering the damage inflicted upon each of the dummies in this scenario, *crashing at a roll angle such as the one we considered is likely to cause a significantly increased damage and fatalities to passengers and should be avoided (through pilots' flight maneuver, for example) if at all possible.*

(4) High speed impact onto a geometrically complicated domain not only causes *severe disintegration of the fuselage*, but also other types of injuries and fatalities such as dismemberments, crushing and squashing of body parts, decapitation, etc.,

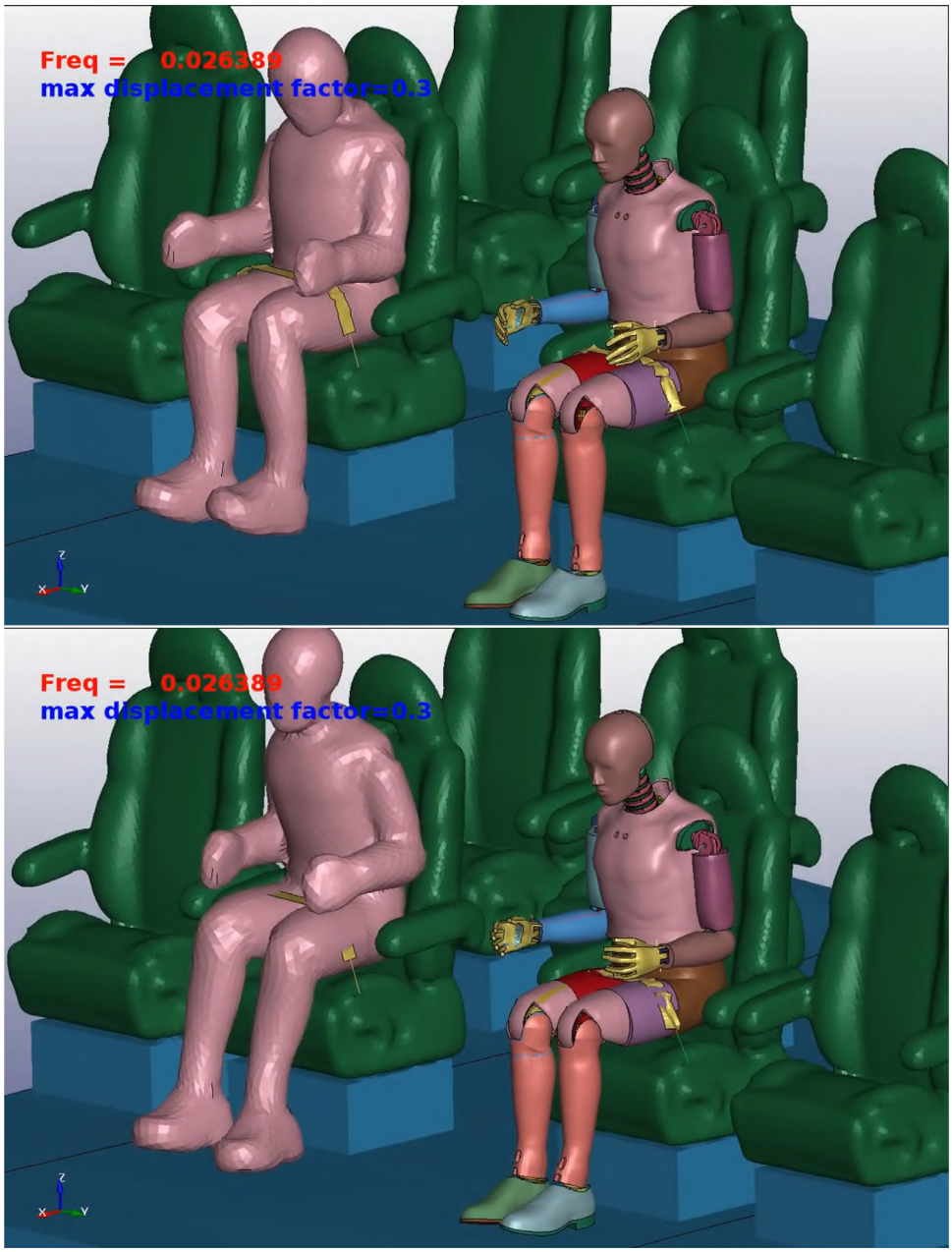

Fig. 37. Mode 292: This mode shows a combination motions of head, neck, spine, and lower leg, potentially causing injuries to all parts. https://drive.google.com/file/d/1Vp0jmdoKTMRjnP4YChWOnE3CP48DH7zw/view?usp=sharing Click graphics or here to play.

which can be seen in the video for Fig. 40. In the worst scenario, the aircraft nearly "pulverizes" such as the Germanwings 9525 [50] and survivability is nonexistent.

Each one of these scenarios has been shown to lead to injuries similar to those seen in automobile crashes, especially with regards to the motion of the neck and head. However, a main difference that is caused by the vertical nature of the drop test is the elongation or compression of the spine in dummies and, therefore, passengers. This extreme jerk caused by impact will likely cause harm to the vertebral column, especially in passengers who are less supported by developed muscle in this region.

In crashes where the nose or tail of the airplane comes in contact with the ground first, the force applied perpendicular to floor of the fuselage will be somewhat absorbed and minimized and will result in injuries more similar to those seen in automobile crashes where the force is applied to the front or rear of the vehicle.

(a)

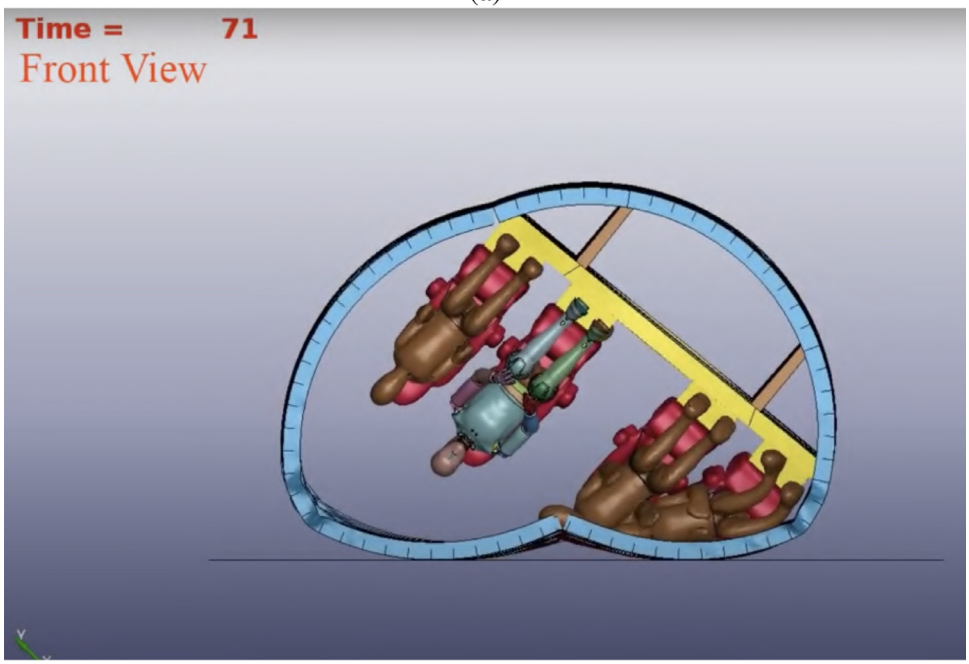

(b)

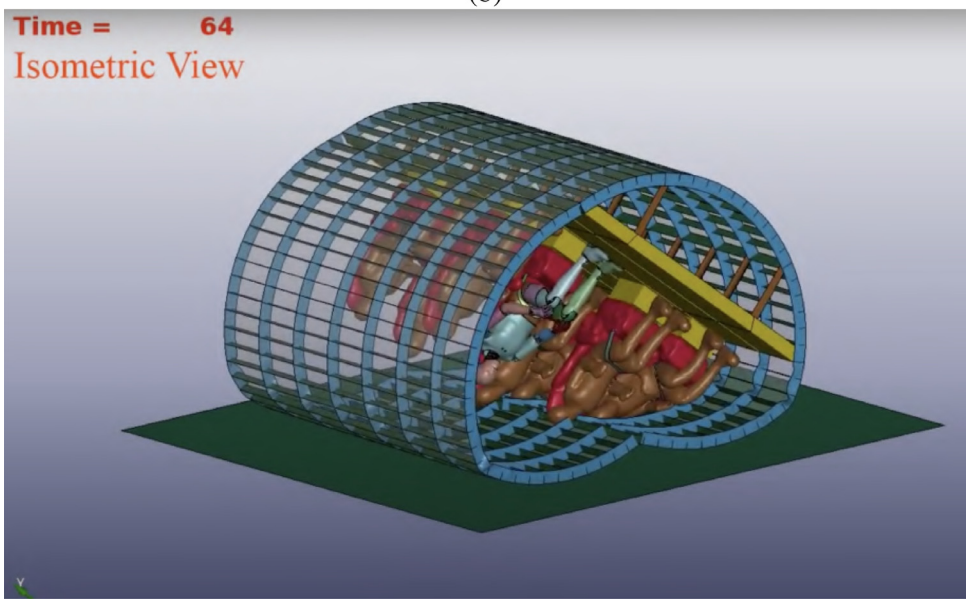

Fig. 38. Results of calculations of the fuselage impact tilted by 135°: (a) front view, (b) isometric projection, transparent perspective.

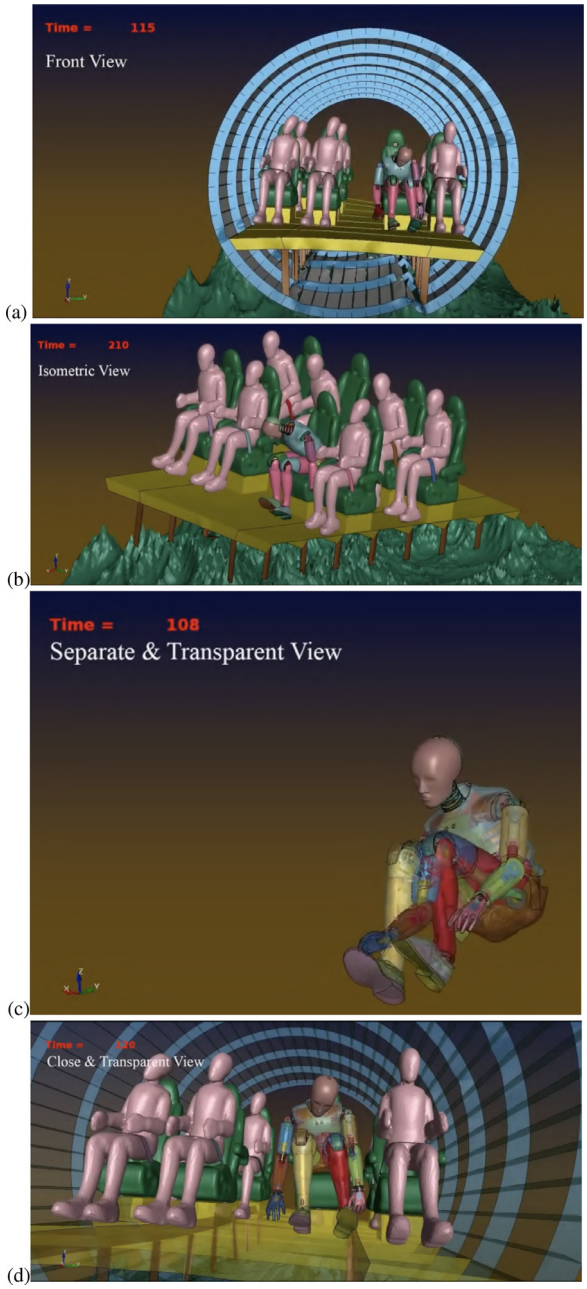

Fig. 39. Drop test on natural fractal terrain at $t = 0.3\,sec$: (a) front view, (b) perspective projection, (c) passenger, (d) bottom view.

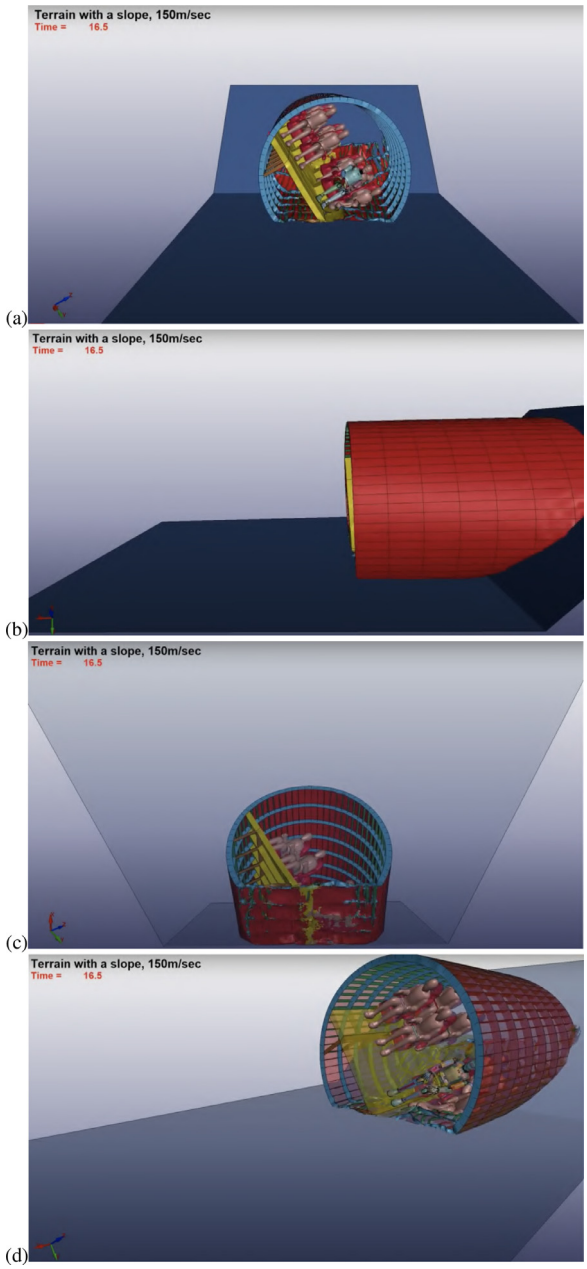

Fig. 40. Drop test on a terrain with a slope, at time t=0.3 sec: front view (a), side view (b), bottom view (c) and transparent view (d).

6. Concluding remarks

Passenger safety and aircraft crashworthiness are two utmost concerns in an airplane crash. These two concerns are inseparably linked to each other. In this paper, we treat them together according to the flowchart in Fig. 41.

We have talked with a prominent aircraft safety inspector and airplane-crash investigator, who is a retiree from National Transportation Safety Board (NTSB). He indicated the challenges in the study of aircraft crashworthiness and survivability. Such a study is *highly sensitive* to the initial and boundary conditions and controls involved that is not unlike the "butterfly effect", namely, a small change in the given conditions and controls could lead to an immensely different crash outcome.

Moreover, he said that during his days, the inspectors/investigators studied an air crash according to the following two doctrines:

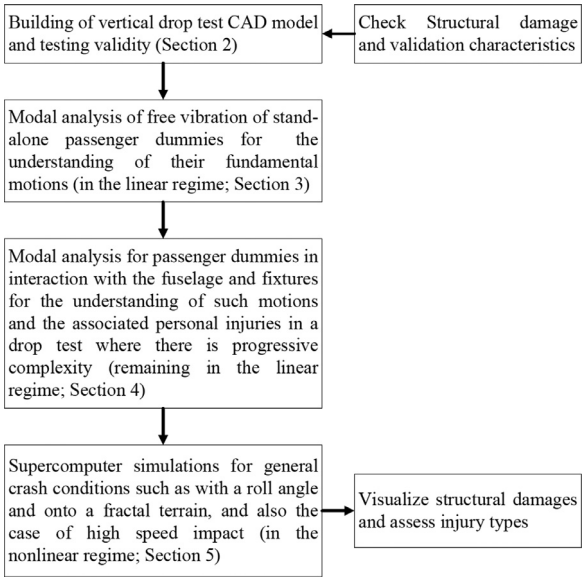

Fig. 41. The conceptual and work flow of our study, aiming at the dual objectives of passenger safety/injury analysis, and aircraft crashworthiness.

(1) If, under the assumptions of low g-forces and no fire inside the aircraft, there was enough space (cubic feet), called *survivable space*, left in the wreckage that allowed an occupant to be not squashed to death in the structural collapse, then the crash was deemed survivable.
(2) Whether any scattered and airborne debris, thrown-off occupants, fixtures (overhead bin materials, broken seats, service carts...) might have compromised the survivable space to cause deaths.

The inspectors/investigators then make recommendations for fixes. Therefore, the survivability hinges on two fundamental concepts: survivable space and airborne projectiles. These could help us build meaningful *metrics* for aircraft crashworthiness and survivability in the future. Nevertheless, at the present time, no quantified metrics have been devised.

We have developed and used various video visualization tools that has helped to see and understand the dynamical behaviors of crash mechanics. This has never been done before, to the best of our knowledge. We hope that these crash test modeling and results have provided a more systematic, rigorous treatment for reference and benchmarking purposes by other researchers. Such work would be particularly useful in the development of new aerospace industry products by computer simulation in lieu of expensive and lengthy hardware and laboratory experiments.

In future work, we wish to make a *full-sized passenger airplane*, equipped with engines, wings, all the supporting structures, cockpit, fuel tank, fixtures, etc., and test it under general crash conditions. Currently, this is yet unreachable because this would exceed our supercomputer capacity at Texas A&M University. Except for this limitation, there are no other reasons why this could not be achieved.

Declaration of Competing Interest

Authors declare that they have no conflict of interest.

Acknowledgments

The work of G. Chen, A. Sergeev and J. Yeh were supported in part by Qatar National Research Fund Grant NPRP #9-166-1-031. J. Yang and C. Wei was supported by a grant from the Chinese Scholarship Council for Ph.D. co-training at Texas A&M University. D. Yang was supported in part by NSFC grant #11871478. S. Xiang was supported in part by NSFC grant #11771454. Marlan O. Scully was partially supported by the Air Force Office of Scientific Research (Award no. FA9550-18-1-0141), Office of Naval Research (Award no. N00014-20-1-2184), Robert A. Welch Foundation (Grant no. A-1261), National Science Foundation (Grant no. PHY-2013771) (new NSF-BSF award), and King Abdulaziz City for Science and Technology (KACST). All coauthors wish to thank Texas A&M Universitys High Performance Research Computing Center for technical assistance and for generous allocation of hours.

Appendix A. Material properties and system parameters of various mechanical components for computer modeling

We first list overall system parameters between our work and experiments in Kumakura, et al.[5,7] in Table A.1.

Table A.1
Parameter listing for various parts (units: kg - mm - ms).

Part	Parameter	Kumakura, et al.[7]	Our simulation
Fuselage	Length	3360	3360
	Diameter	2880	2880
	Total weight	1510	1512.39
	Impact velocity	6.1	6.1
Fuselage	Thickness	Unknown	2.5
skin	Weight	Unknown	212.48
Ring-	Thickness	Unknown	2
stiffener	Weight	Unknown	39.37
Stringer	Thickness	Unknown	2
	Weight	Unknown	78.02
Seat	Thickness	Unknown	4
	Weight	Unknown	52.20
Floor	Thickness	Unknown	3
	Weight	Unknown	107.31
Strut	Thickness	Unknown	3
	Weight	Unknown	14.68
Rubber	Weight	NA/Unknown	7×80.46
dummy	Mass density	NA/Unknown	1.400e−06
LS-DYNA ATD	Weight	NA/Unknown	1×79.60

Table A.2
Properties of aluminum, as defined by the keyword *MAT_PLASTIC_KINEMATIC. Units are based on mm/ms/kg.

Property	Variable	Value
Title	TITLE	Aluminium Alloy 7075-T6
Mass density	RO	3.0×10^{-6}
Young's modulus	E	70.0
Poisson's ratio	PR	0.35
Yield stress	SIGY	0.47
Tangent modulus	ETAN	0.70
Hardening parameter	BETA	0.11

The parameters for individual components are given in the subsequent sections.

As shown in Fig. 2, there are a total of ten different parts marked by component names. In this Appendix, we list their material properties and system parameters. These values, used in combination with the LS-DYNA computer codes to be given in Appendix B, will enable the interested reader to reproduce or verify our computational results. **A.i Fuselage and fixtures**

A1. Fuselage skin

The fuselage has a cylindrical shape; see Fig. A.1.

The fuselage skin as well as other metal parts except passengers are assumed to be made of aluminum; see Table A.2. The keyword is *MAT_PLASTIC_KINEMATIC.

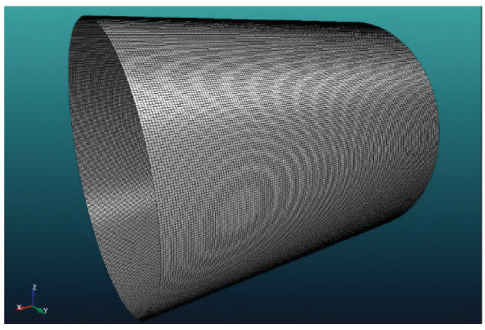

Property	Value
Radius	1.44 m
Length	3.36 m
Thickness	2.5 mm
Density	2796 kg/m^3
Area	30.40 m^2
Mass	212.48 kg
Number of finite element	77616

Fig. A.1. The cylindrical skin of the fuselage section and system parameters.

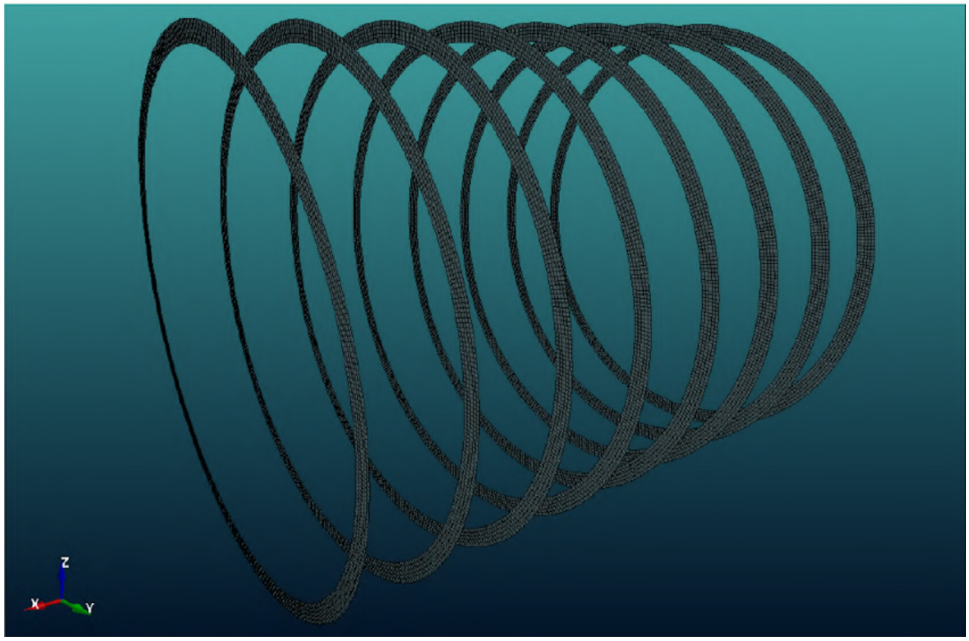

Fig. A.2. Ring-stiffeners of the fuselage section designed to improve its stiffness.

Table A.3
Parameters of ring-stiffeners.

Property	Inner radius	Outer radius	Width	Thickness	Density	# of ribs	Area	Mass	Number of finite elements
Value	1.339 m	1.440 m	100.8 mm	2.0 mm	2796 kg/m^3	8	7.04 m^2	39.37 kg	18,480

Table A.4
Properties of stringers.

Property	Value
Length	3.36 m
Width	60.48 mm or 100.8 mm
Thickness	2.0 mm
Density	2796 kg/m^3
Number of stringers	66
Number of stringers of width 60.48 mm	62
Number of stringers of width 100.8 mm	4
Stringer No. corresponding to $phi = 0$	17
Wider stringers connected to floor	38 and 61
Wider stringers connected to struts	44 and 55
Area	13.95 m^2
Mass	78.02 kg
Number of finite elements	34 608

A2. Ring-stiffeners

Ring-stiffeners have the shape of an annulus, as shown in Fig. A.2. Twelve of them are used. Material properties and system parameters are given in Table A.3.

A3. Stringers

Stringers run longitudinally. They have a rectangular shape, with length 3.36 m. There are 62 stringers of width 57.6 mm and 4 wider stringers of width 115 mm that are connected to a floor and struts; cf. Fig. A.3 and Table A.4.

A4. Floor

The floor has an approximate shape of a rectangle. It is made of aluminum; cf. Table A.5.

Table A.5
Properties of floor.

Property	Length	Width	Thickness	Density	Number of support beams	Height of support beam	Length of support beam on mid-level	Area	Mass	Number of finite elements
Value	3.36 m	2.63 m	3.0 mm	3000 kg/m^3	8	110.4 mm	2.44 m	10.04 m^2	90.40 kg	27 328

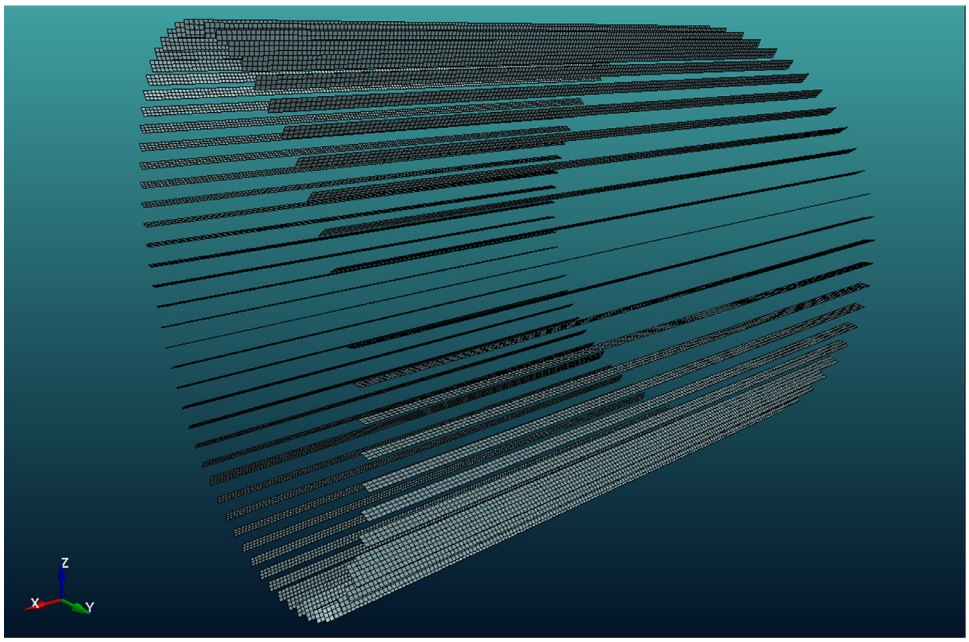

Fig. A.3. Stringers of the fuselage section designed to gain additional stiffness of the fuselage.

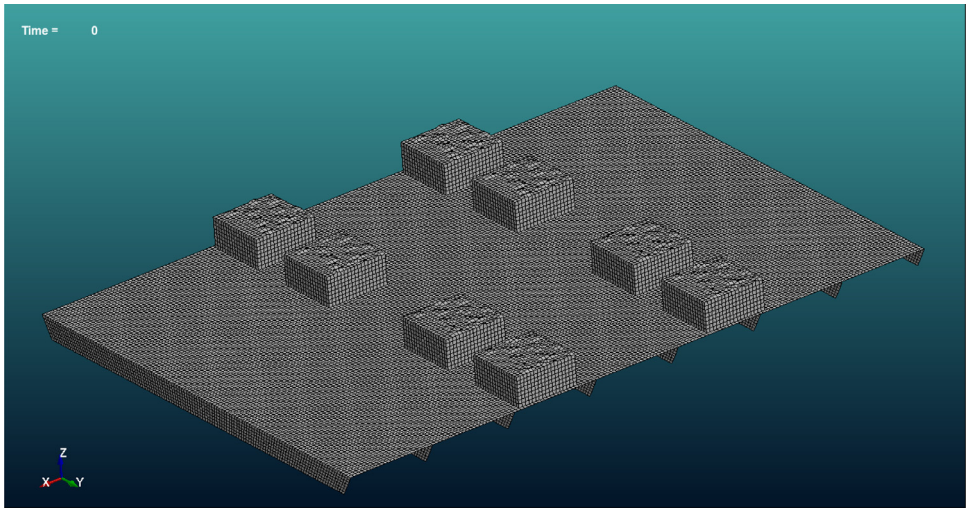

Fig. A.4. Floor with supporting beams and boxes to support seats.

Table A.6
Properties of struts (units: kg - mm - ms).

Property	Height	Width	Thickness	Density	Area	Mass	Number of finite elements
Value	563.91	80	3	2.796e−06	1.750e+06	14.68	4992

A5. Struts

Struts are the beam-like supporting elements that prevent the sagging of the floor under weight of passengers. The material is made of Aluminium Alloy 7075-T6, with keywords `*SECTION_SHELL_TITLE` and `*MAT_PLASTIC_KINEMATIC_TITLE`. Also, see Table A.6 for system parameters.

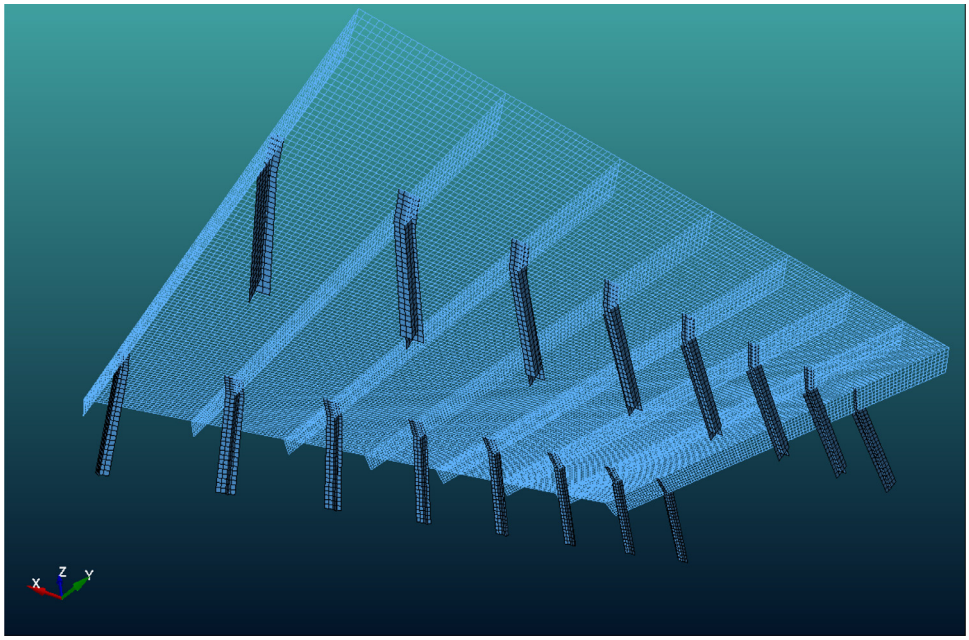

Fig. A.5. Struts supporting the floor.

Table A.7
Properties of struts.

Property	Value	Property	Value
Half-width	36.9 mm	Number of X-shaped struts	12
Hight	435.8 mm	Number of T-shaped struts	4
Thickness	3.0 mm	Area	1.10 m^2
Density	3000 kg/m^3	Mass	9.88 kg
Distance between struts in pairs	1.34 m		
Number of struts	16	Number of finite elements	3032

Table A.8
Properties of seats.

Property	Value	Property	Value
Width	546.4 mm	Height on the level of seat surface	460 mm
Height	1160 mm	Thickness of stander on top level	100 mm
Depth	400 mm	Thickness of stander on bottom level	200 mm
Density	3000 kg/m^3	Thickness of cushion	80 mm
Area	17.93 m^2	Distance between seats in rows	600 mm
Mass	107.55 kg	Spacing between double seats in a row	156.1 mm
Number of rows	2	Distance between the last row of seats and the rear edge of the floor	920 mm
Number of seats in a row	4	Distance between the window seats and the edge of the floor	19.5 mm
Total number of seats	8	Thickness of material	2.0 mm
Number of finite elements 45,744			

A6. Seats

The seats consist of of a curved part attached to a rectangular box. The seats are arranged in two rows of 4 seats, 8 seats in total; cf. Fig. A.6.

A7. Seatbelts

The seatbelts have rectangular shapes and are attached to the seats as shown on; cf. Fig. A.7 and Table A.9.

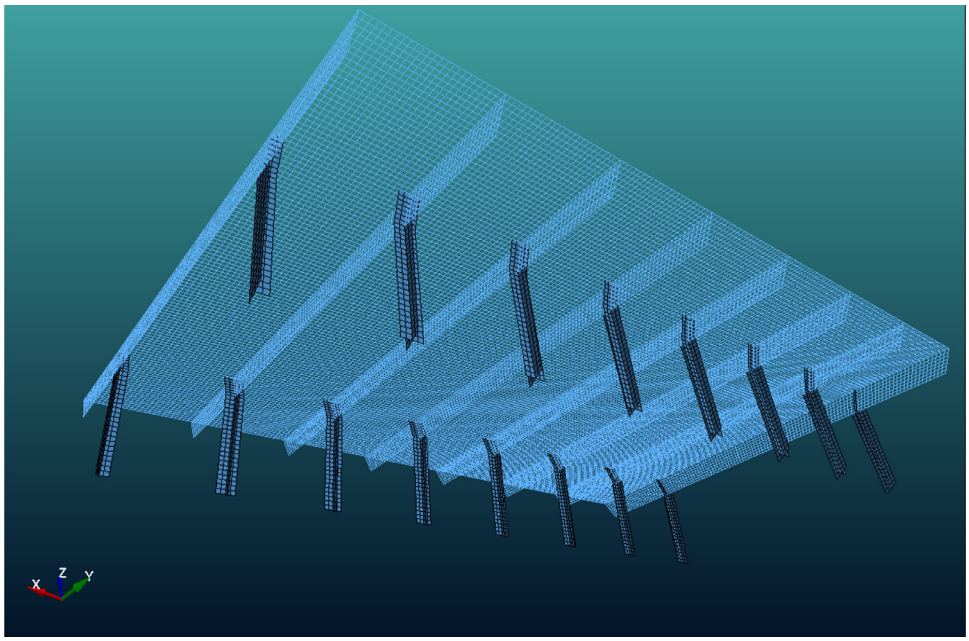

Fig. A.6. Seats attached to the floor.

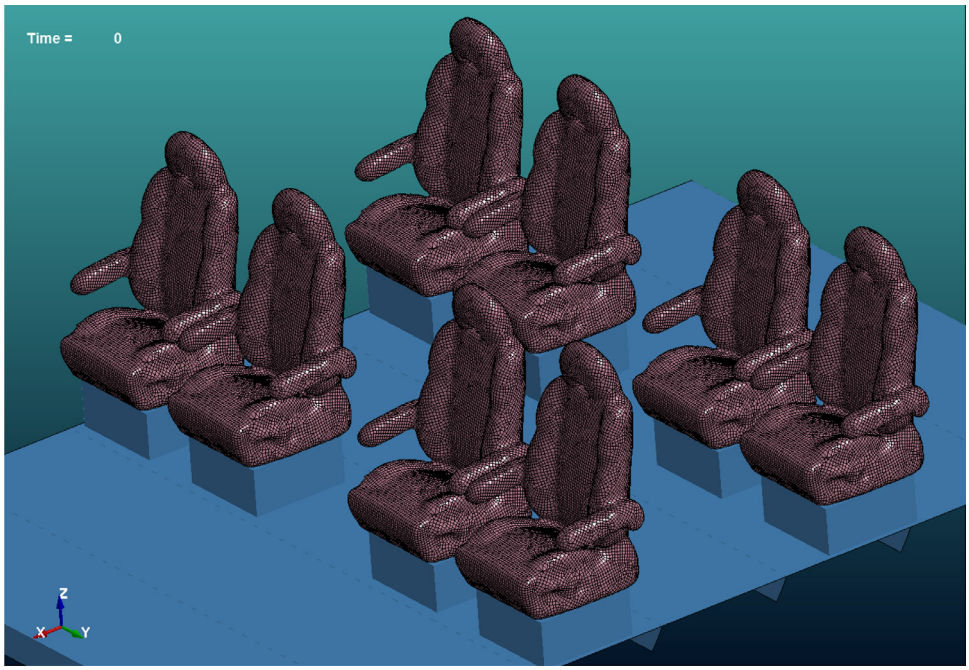

Fig. A.7. Seatbelts attached to the seats.

Table A.9
Properties of seatbelts.

Property	Value	Property	Value
Distance from bottom edge to the seat	320 mm	Thickness	2.0 mm
Distance from top edge to the seat	400 mm	Density	7830 kg/m^2
Ribbon width	80 mm	Area	0.81 m^2
Lateral width	351.2 mm	Mass	12.69 kg
Width in forward direction	360 mm	Number of finite elements	2 048
Total number of seatbelts	8		

Table A.10
Properties of material of seatbelts, as defined in the card *MAT_FABRIC. Units are based on mm/ms/kg.

Property	Title	Mass density	Young's modulus	Poisson's ratio	Yield stress	Tangent modulus
Variable	TITLE	RO	E	PR	SIGY	ETAN
Value	Shell belt material	7.83×10^{-6}	200.0	0.3	0.15	2.0

Table A.11
Properties of material of passenger dummies, as defined in the card *MAT_LOW_DENSITY_FOAM, in mm/ms/kg. Other parameters are assigned to default values.

Property	Variable	Value
Mass density	RO	3.0×10^{-6}
Young's modulus	E	0.005
Nominal stress versus strain	Loaded curve	See Fig. A.13
Tension cut-off stress	TC	10.0
Hysteretic unloading factor	HU	1.0

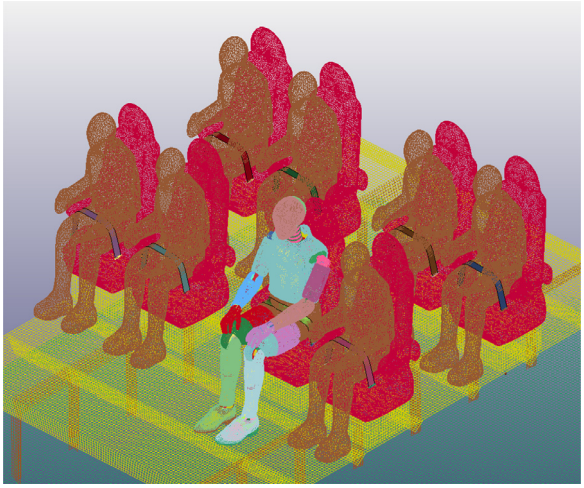

Fig. A.8. Pad on the ground which the fuselage hits when it is dropped to the ground.

A8. Ground pad

The pad on the ground is considered as a rectangle of dimensions 3.60×4.22 m. The initial distance from the pad to the fuselage is 0.25 m. The material is rigid, i.e. deformations are not allowed. The number of finite elements is 37980; cf. Fig. A.8.

A9. Initial conditions

The initial velocity is -5.684 m/s and is directed vertically. The free fall acceleration is 9.81 m/s^2. The velocity reaches -6.1 m/s when the fuselage hits the ground (at $t = 42$ ms), or approximately 20 feet per second. **Results** Calculations were done up to maximal time 0.5 s, with an output interval of 1 ms, on 84 processors, with double precision. The calculation time is around 53 h. **A.ii Design of a rubber dummy** Here, we briefly describe how we designed our own rubber dummy. We start from the standard LSTC Hybrid III 50 Percentile ATD as used in Section 3 as a prototype.

First, the model was positioned as it is shown in the left panel of Fig. A.10. Then, we used a mesh processing software MeshLab to make a more uniform mesh. For this purpose, the mesh was uniformly resampled, see Fig. A.10. Note that arms are not fused with the body in the new model.

Finally, we tried to apply several mesh transformations, or filters, see Figs. A.11 and A.12. For material properties see Table A.11.

We found that the filter "ISO parametrization remeshing" gives the most uniform mesh, and this mesh was used to construct a three-dimensional tetrahedral mesh in LS-PREPOST.

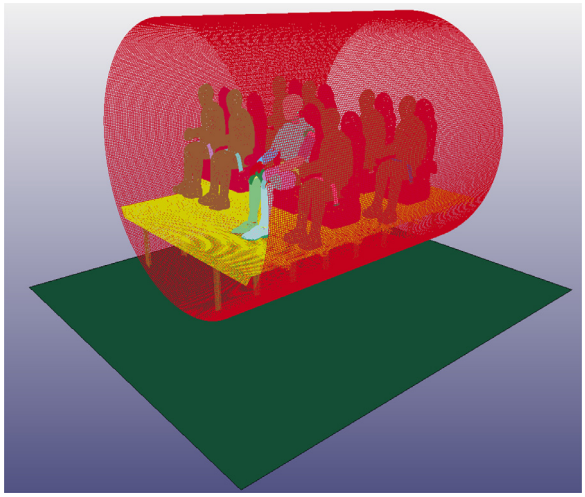

Fig. A.9. Passengers placed on seats.

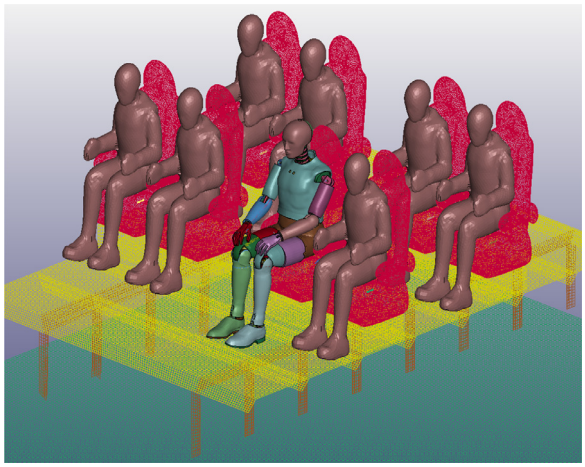

Fig. A.10. Resampling mesh of a dummy. Left panel is the original mesh, right panel is the uniformly resampled mesh.

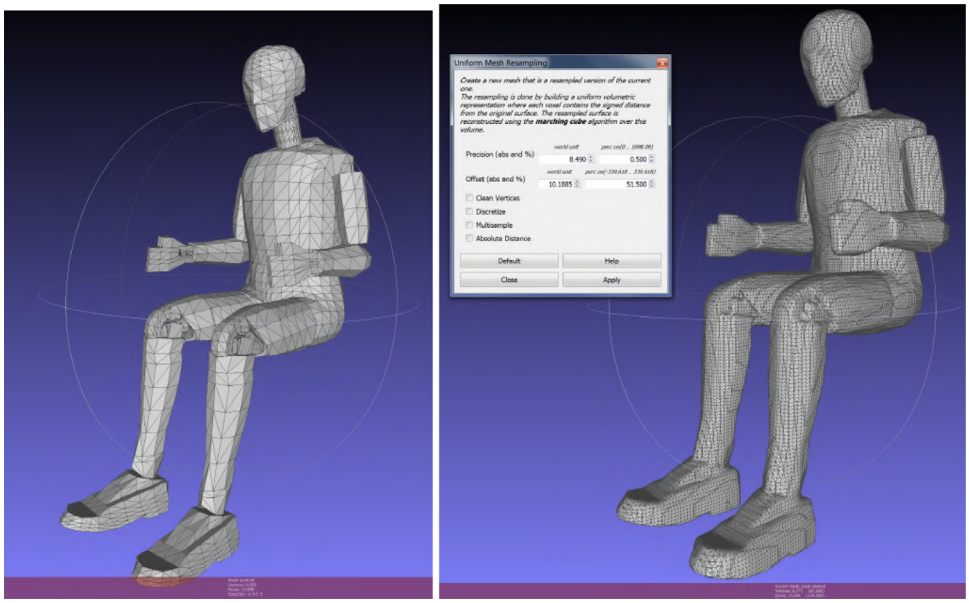

Fig. A.11. Trying mesh transformations to make it more smooth. Left panel is Taubin smoothing, right panel is fractal displacement.

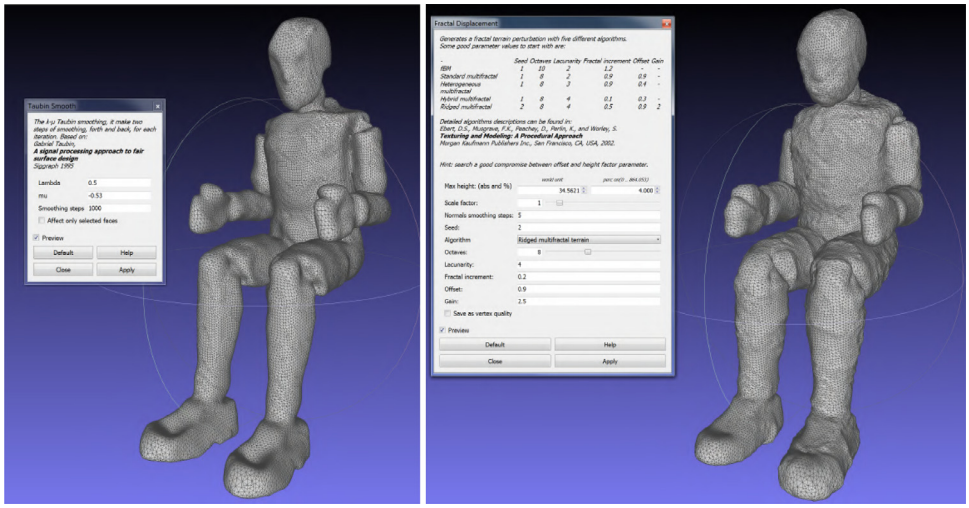

Fig. A.12. Trying mesh transformations to make it more smooth. Left panel is Laplacian smoothing, right panel is ISO parametrization remeshing.

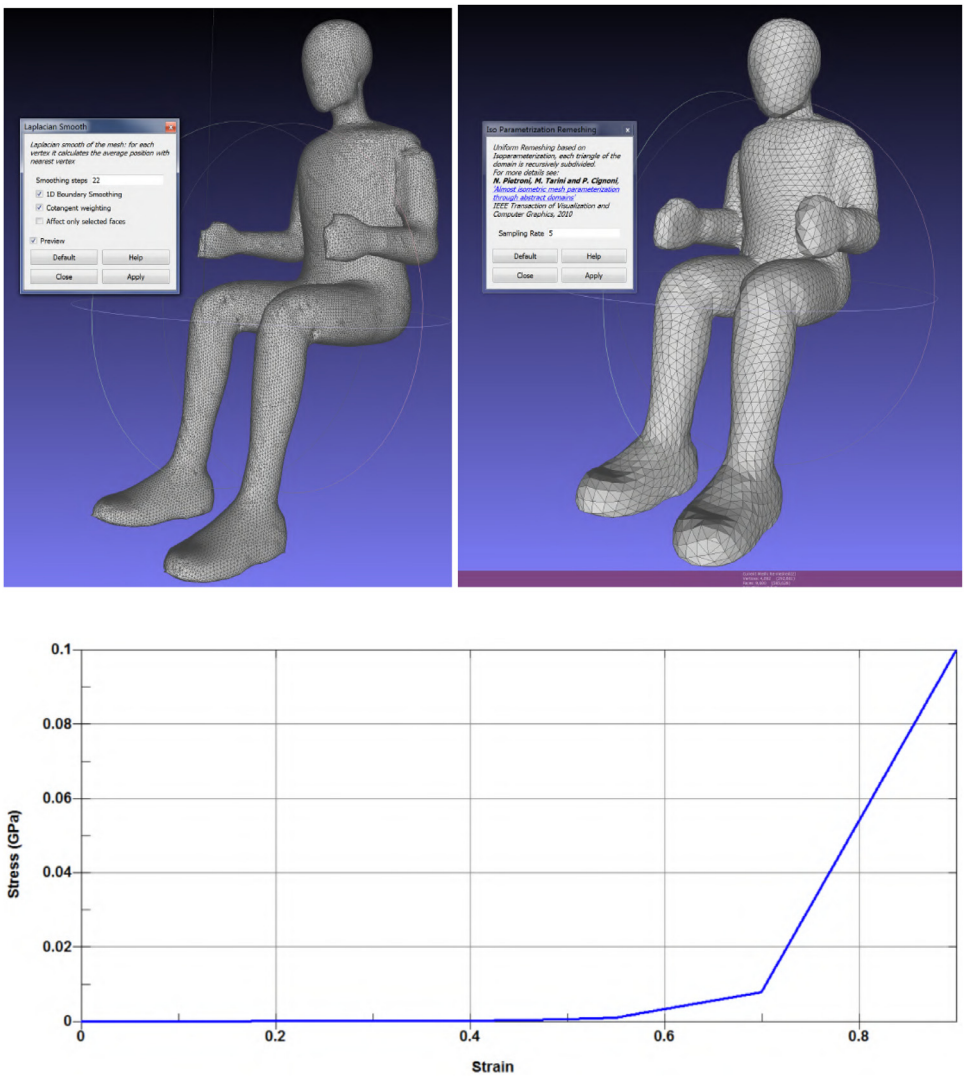

Fig. A.13. The curve for "nominal stress versus strain" in Table A.11. For our rubber dummy made of artificial rubber, the vertical scale is increased 50 times.

Appendix B. LS-DYNA computer codes for crash simulations

Here, we present the rudiments of our LS-DYNA computer codes in order to facilitate the reader who is interested in computational applications. **B.i Modal Analysis**

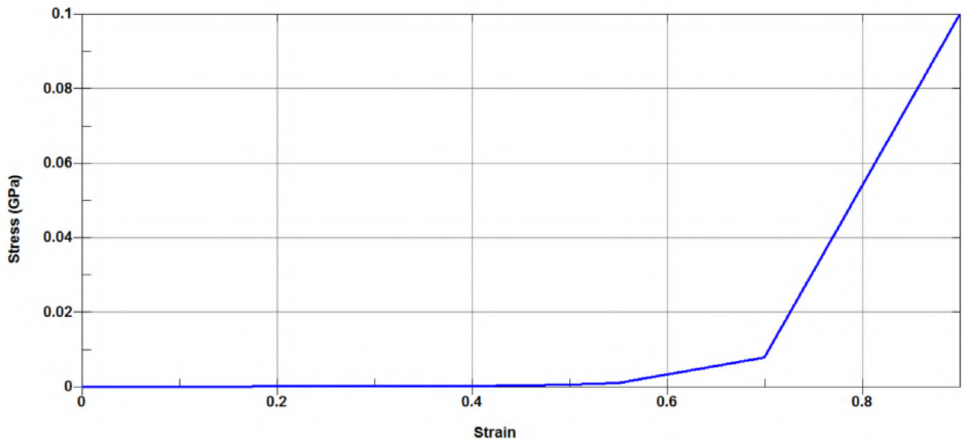

Fig. A.13. Continued

```
*KEYWORD
*TITLE
$# Mode shape computation
$ Activate implicit analysis
*CONTROL_IMPLICIT_EIGENVALUE
$# neig  center  lflag  lftend  rflag  rhtend  eigmth  shfscl
     100     0.0      0     0.0      0     0.0       2     0.0
$# isolid  ibeam  ishell  itshell  mstres  evdump  mstrscl
         0      0       0        0       1       0    0.001
$ Define parameters for implicit calculations
*CONTROL_IMPLICIT_GENERAL
$# imflag  dt0  imform  nsbs  igs  cnstn  form  zero_v
         1  1.0       2     0    2      0     0       0
$ Activate implicit eigenvalue analysis
*CONTROL_IMPLICIT_SOLUTION
$# nsolvr  ilimit  maxref  dctol  ectol  rctol  lstol  abstol
         1       0       0    0.0    0.0    0.0    0.0     0.0
$# dnorm  diverg  istif  nlprint  nlnorm  d3itctl  cpchk
         2       1      0        0       2        0      0
$# arcctl arcdir arclen arcmth arcdmp arcpsi arcalf arctim
         0      0    0.0      1      2      0      0      0
$# lsmtd  lsdir  irad  srad  awgt  sred
         4      2   0.0   0.0   0.0   0.0
*CONTROL_CONTACT
$# slsfac rwpnal islchk shlthk penopt thkchg orien enmass
       0.1     1.0      0      0      0      0      2       0
$# usrstr  usrfrc  nsbcs  interm  xpene  ssthk  ecdt  tiedprj
         0       0      0       0    0.0      1     0        0
$# sfric  dfric  edc  vfc  th  th_sf  pen_sf
      0.0    0.0  0.0  0.0  0.0     0.0     0.0
$# ignore  frceng  skiprwg  outseg  spotstp  spotdel  spothin
         1       0        0       0        0        0      0.0
$# isym  nserod  rwgaps  rwgdth  rwksf  icov  swradf  ithoff
       0       0       1     0.0    1.0     0     0.0       0
$# shledg  pstiff  ithcnt  tdcnof  ftall  unused  shltrw  igactc
         0       0       0       0      0             0.0       0
*CONTROL_OUTPUT
$# npopt  neecho  nrefup  iaccop  opifs  ipnint  ikedit  iflush
         1       3       0       1    0.0       0    9000       0
$# iprtf  ierode  tet10s8  msgmax  ipcurv  gmdt  ip1dblt  eocs
       0       0        2       0       0   0.0        0     0
$# tolev  newleg  frfreq  minfo  solsig  msgflg  cdetol
       2       0       1      0       0       0    10.0
$# phschng  demden  icrfile  spc2bnd  -  shlsig  hisnout
         0       0        0        0  0       0        0
$# insf  isolsf  ibsf  issf
      0       0     0     0
$ Define termination time
*CONTROL_TERMINATION
$# endtim  endcyc  dtmin  endeng  endmas  nosol
    800.0        0    0.3  0.01.000000E8       0
$ Define time step
*CONTROL_TIMESTEP
$# dtinit  tssfac  isdo  tslimt  dt2ms  lctm  erode  ms1st
5.00000E-4   0.8  02.00000E-4      0.0     0      1      0
$# dt2msf dt2mslc imscl unused unused rmscl unused ihdo
        0.0      0     0                0.0             0
$ Set output parameters
*DATABASE_BINARY_D3PLOT
$# dt  lcdt  beam  npltc  psetid
   5.0     0     0      0       0
$# ioopt  rate  cutoff  window  type  pset
       0   0.0     0.0     0.0     0     0
$ Define contact
*CONTACT_ERODING_SINGLE_SURFACE_MPP_ID
$# cid  title
      2 Universal contact
$# ignore   bcket  lcbckt  ns2trk  inititr  parmax
   unused  cparm8
        0     200       0       3        2  1.0005
                0
$#   ssid  msid  sstyp  mstyp  sboxid  mboxid  spr  mpr
52400103     0      2      0       0       0    0    0
$# fs  fd  dc  vc  vdc  penchk  bt  dt
  0.2 0.2 0.2 0.2  0.2       0  0.01.00000E20
$# sfs  sfm  sst  mst  sfst  sfmt  fsf  vsf
    1.0  1.0  0.0  0.0  1.0   1.0  1.0  1.0
$# isym  erosop  iadj
       0       0     0
$# soft  sofscl  lcidab  maxpar  sbopt  depth  bsort  frcfrq
      1     0.1       0   1.025    2.0      2      0       1
$ Define parts, sections, and materials
*SECTION_SHELL_TITLE
shell-2.0
  2    2   1.0    2  1.0    0    0   1
2.0  2.0  2.0  2.0  0.0  0.0  0.0  0
*PART
Stringers
3  2  1  0  1  0  0  0
*PART
Floor
4  3  1  0  1  0  0  0
*SECTION_SHELL_TITLE
shell-3.0
  3    2   1.0    2  1.0    0    0   1
3.0  3.0  3.0  3.0  0.0  0.0  0.0  0
*PART
Struts
5  3  1  0  1  0  0  0
*PART
Seat cushions
6  2  1  0  1  0  0  0
*PART
Seatbelts
20  20  20  0  0  0  0  0
*SECTION_SHELL_TITLE
seatbelt
 20    2  0.0    0  1.0     0    0  1
2.0  2.0  2.0  2.0  0.0  0.0  0.0  0
*MAT_PIECEWISE_LINEAR_PLASTICITY_TITLE
shell belt material
 207.83000E-6   200.0   0.3   0.15   2.01.00000E21   0.0
0.0             0.0     0     0     0.0
0.0             0.0   0.0   0.0   0.0   0.0       0.0   0.0
```

```
0.0         0.0     0.0   0.0   0.0   0.0         0.0   0.0
*PART
Dummies
50   50   50   0   0   0   0   0
*SECTION_SOLID_TITLE
Solid
50   10   0
*MAT_LOW_DENSITY_FOAM
 503.00000E-6  0.173    50   10.0   1.0   0.0   0.0
0.0          0.0     0.0   0.0   0.0   0.0   0.0
```

B.ii $150\ m/s$ crash simulation (Subsection 5.3)

```
*KEYWORD
*TITLE
$# title
On the slope, 100 m/sec
*CONTROL_ACCURACY
$       0     2
$#      osu      inn      pidosu      iacc
          1        4           0         0
*CONTROL_TERMINATION
$#  endtim endcyc     dtmin     endeng     endmas     nosol
     500.0      0       0.3  0.01.000000E8          0
*CONTROL_TIMESTEP
$#   dtinit    tssfac      isdo     tslimt     dt2ms      lctm
    erode     ms1st
       0.0       0.8          04.00000E-4       0.0         0
         1         0
$# dt2msf dt2mslc     imscl     unused     unused     rmscl
   unused      ihdo
       0.0         0         0                              0.0
                   0
*DATABASE_GLSTAT
$#       dt    binary      lcur     ioopt
        0.1         0         0         1
*DATABASE_BINARY_D3PLOT
$#       dt      lcdt      beam      npltc     psetid
        0.5         0         0         0          0
$#   ioopt      rate    cutoff    window      type      pset
         0       0.0       0.0       0.0         0         0
$ Define damping
*DAMPING_GLOBAL
$#     lcid    valdmp       stx       sty       stz       srx       sry       srz
          2       0.0       0.0       0.0       0.0       0.0       0.0       0.0
$ Define initial velocity
*INITIAL_VELOCITY_GENERATION
$#nsid/pid      styp omega        vx        vy        vz  ivatn     icid
           1         1     0.0     0.0 129.9038  -75.0      0        0
$#         xc        yc        zc        nx        ny        nz     phase     irigid
        0.0       0.0       0.0       0.0       0.0       0.0         0          1
   52400102         1       0.0       0.0 129.9038  -75.0         0          0
        0.0       0.0       0.0       0.0       0.0       0.0         0          1
*DATABASE_BINARY_RUNRSF
$#      cycl      nr beam npltc psetid
    10000.0       0    0     0      0
$ Define contact between various parts
*CONTACT_ERODING_SINGLE_SURFACE_MPP_ID
$#       cid   title
          35 fuselage+pad
$#  ignore  bcket  lcbckt  ns2trk  inititr  parmax  cparm8
       0     200       0       3        2  1.0005       0
$#     ssid    msid    sstyp    mstyp  sboxid  mboxid     spr     mpr
          2       0        2        0       0       0       0       0
$#       fs      fd       dc       vc      vdc  penchk      bt      dt
      0.2     0.2      0.2      0.2      0.2       0 0.01.00000E20
$#      sfs     sfm      sst      mst     sfst     sfmt     fsf     vsf
      1.0     1.0      0.0      0.0      1.0      1.0     1.0     1.0
$#    isym  erosop     iadj
        0       1        0
$#    soft  sofscl  lcidab  maxpar  sbopt  depth  bsort  frcfrq
       1     0.1       0   1.025    2.0      2      0       1
*SET_PART_LIST_TITLE
Everything
$#     sid     da1     da2     da3     da4  solver
         2     0.0     0.0     0.0     0.0  MECH
$#    pid1    pid2    pid3    pid4    pid5    pid6    pid7    pid8
       1       2       3       4       5       6      21      22
      23      24      27      28      29      30      31      32
      33      34      35      36      50     100       0       0
*CONTACT_AUTOMATIC_SURFACE_TO_SURFACE_ID
$#     cid     title
        36
$#    ssid     msid    sstyp    mstyp  sboxid  mboxid     spr     mpr
50100003        1        2        2       0       0       1       1
$#      fs      fd       dc       vc      vdc  penchk      bt      dt
     0.3     0.3      0.0      0.0     20.0       0 0.01.00000E20
$#     sfs     sfm      sst      mst     sfst     sfmt     fsf     vsf
     1.0     1.0      0.0      0.0      1.0      1.0     1.0     1.0
$#    soft  sofscl  lcidab  maxpar  sbopt  depth  bsort  frcfrq
       2     0.0       0     0.0     0.0      0      0       0
$# penmax  thkopt  shlthk  snlog   isym  i2d3d  sldthk  sldstf
       0.0       0       0       0      0      1     0.0     0.0
$#    igap  ignore  dprfac  dtstif  flangl  cid_rcf
       1       0  0.05.00000E-4     0.0        0
*SET_PART_LIST
$#     sid     da1     da2     da3     da4  solver
 50100003     0.0     0.0     0.0     0.0  MECH
*CONTACT_ERODING_SINGLE_SURFACE_MPP_ID
$#     cid   title
          34dynadummy+ground
$# ignore  bcket  lcbckt  ns2trk  inititr  parmax  cparm8
       0     200       0       3        2  1.0005       0
$#     ssid    msid    sstyp    mstyp  sboxid  mboxid     spr     mpr
52400107        0        2        0       0       0       0       0
$#       fs      fd       dc       vc      vdc  penchk      bt      dt
     0.2     0.2      0.2      0.2      0.2       0 0.01.00000E20
$#      sfs     sfm      sst      mst     sfst     sfmt     fsf     vsf
     1.0     1.0      0.0      0.0      1.0      1.0     1.0     1.0
$#    isym  erosop     iadj
        0       1        0
```

```
$#    soft  sofscl lcidab maxpar  sbopt  depth  bsort frcfrq
         1     0.1      0  1.025    2.0      2      0      1
$ Define part set
*SET_PART_LIST_TITLE
Entire Dummy+Ground
$#     sid    da1    da2    da3    da4  solver
 52400107    0.0    0.0    0.0    0.0 MECH
*PART
Fuselage skin
         1      5      1      0      1      0      0      0
*SECTION_SHELL_TITLE
shell-2.5
         5      2    1.0      2    1.0      0      0      1
       2.5    2.5    2.5    2.5    0.0    0.0    0.0      0
*MAT_PLASTIC_KINEMATIC_TITLE
Aluminium Alloy 7075-T6
 12.79570E-6   70.0    0.33   0.47    0.7   0.11
         0.0    0.0    0.1    0.0
*HOURGLASS
         1      1    0.1      0    1.5   0.06    0.1    0.1
$ Define gravitational acceleration
*LOAD_BODY_Y
      lcid      sf  lciddr      xc      yc      zc     cid
         1  -0.866       0     0.0     0.0     0.0       0
*LOAD_BODY_Z
$#    lcid      sf  lciddr      xc      yc      zc     cid
         1     0.5       0     0.0     0.0     0.0       0
*DEFINE_CURVE
$#    lcid      sidr       sfa       sfo      offa      offo    dattyp      lcint
         1         0       1.0       1.0       0.0       0.0         0          0
$#      a1        o1
       0.0   0.00981
   1000000   0.00981
*DEFINE_CURVE_TITLE
DampingCurve
$#    lcid      sidr       sfa       sfo      offa      offo    dattyp      lcint
         2         0       1.0       1.0       0.0       0.0         0          0
$#      a1        o1
       0.0       0.0
      17.0       0.0
      18.0     0.003
   10000.0     0.003
```

Control of time step

In our earlier attempts, the calculations frequently became stuck by increasingly small time steps at the moment when deformations of the fuselage become large. It occurs because several mesh elements become extremely deformed, and in order to avoid negative volumes or the divergence, the time step decreases to very small values ($\sim 10^{-7}\, msec$). Here, we perform several steps to avoid this phenomenon.

1. The parameter "Failure strain for eroding elements" (FS) in the card `*MAT_PLASTIC_KINEMA-TIC` was set to 0.1. Our previous value was often 0.01, but it seems that 0.03 is more realistic.

2. We added a card `*MAT_ADD_EROSION` with "Volumetric strain at falure" (VOLEPS) equal to 0.1 and "Share strain at failure" (EPSSH) equal to 0.1. It allows to delete very deformed elements that were somehow missed by a standard failure strain criterium for deletion.

3. In the card `*CONTROL_TERMINATION`, we set "Reduction factor for the initial time step size to determine minimum time step" (DTMIN) to 0.3. It forced the time step to be always larger than the initial time step times 0.3.

References

[1] Barnett A. Cross-national differences in aviation safety records. Transp Sci 2010;44(3):322–32. doi:10.1287/trsc.1090.0313.
[2] Fasanella E, Hayduk R, Robinson M, Widmayer E. Analysis of a transport fuselage section drop test. Res Struct Dyn 1984:347–68.
[3] Fasanella EL, Widmayer E, Robinson MP. Structural analysis of the controlled impact demonstration of a jet transport airplane. J Aircraft 1987;24(4):274–80. doi:10.2514/3.45437.
[4] Fasanella EL, Carden HD, Boitnott RL, Hayduk RJ. A review of the analytical simulation of aircraft crash dynamics. NASA Technical Memorandum (TM) 1025951990.
[5] Minegishi M, Kumakura I, Iwasaki K, Shoji H, Yoshimoto N, Terada H, et al. Vertical drop test of a YS-11 fuselage section. JSASS 2003;51(594):354–63. doi:10.2322/jjsass.51.354. English translation in Kumakura, I., Minegishi, M., Iwasaki, K., Shoji, H., Miyaki, H., Yoshimoto, N., "Summary of Vertical Drop Test of YS–11 Transport Fuselage Sections". *SAE Transactions, Section 1: Journal of Aerospace* Vol. 112, 2003, pp. 531–540.
[6] Iwasaki K, Kumakura I, Minegishi M, Shoji H, Yoshimoto N, Miyaki H, et al. Vertical drop test of a YS-11 fuselage section (part 2). JSASS 2003;51(599):675–82. doi:10.2322/jjsass.51.675.
[7] Kumakura I. Research plan at NAL on drop test of fuselage structure of YS-11 turbo-prop transport aircraft. In: International aircraft fire and cabin safety research conference; 2001.
[8] Mou H, Zou T, Feng Z, Ren J. Crashworthiness simulation research of fuselage section with composite skin. Procedia Eng 2014;80:59–65. doi:10.1016/j.proeng.2014.09.060.
[9] Liu X, Guo J, Bai C, Sun X, Mou R. Drop test and crash simulation of a civil airplane fuselage section. Chin J Aeronaut 2015;28(2):447–56. doi:10.1016/j.cja.2015.01.007.

[10] Delsart D, Portemont G, Waimer M. Crash testing of a CFRP commercial aircraft sub-cargo fuselage section. Procedia Struct Integr 2016;2:2198–205. doi:10.1016/j.prostr.2016.06.275.
[11] Marulo F, Guida M, Di Caprio F, Ignarra M, Lamboglia A, Gambino B. Fuselage crashworthiness lower lobe dynamic test. Procedia Eng 2016;167:88–96. doi:10.1016/j.proeng.2016.11.678.
[12] Paz J, Díaz J, Romera L. Crashworthiness analysis and enhancement of aircraft structures under vertical impact scenarios. J Aircraft 2020;57(1):3–12. doi:10.2514/1.C035435.
[13] Woodson MB, Johnson ER, Haftka RT. Optimal design of composite fuselage frames for crashworthiness. Int J Crashworthiness 1996;1(4):369–80.
[14] Kumakura I, Minegishi M, Iwasaki K. Impact simulation of simplified structural models of aircraft fuselage. In: 2000 world aviation conference; 2000. p. 5586. doi:10.2514/6.2000-5586.
[15] Abramowitz A, Vu T, Smith T, et al. Vertical Drop Test of a Narrow-Body Transport Fuselage Section with a Conformable Auxiliary Fuel Tank Onboard Tech. Rep.. United States Federal Aviation Administration; 2000.
[16] Kindervater CM, Johnson AF, Kohlgrüber D, Lützenburger M, Pentecote N. Crash and impact simulation of aircraft structures-hybrid and fe based approaches. In: European congress on computational methods in applied sciences and engineering. Barcelona, Spain: ECCOMAS; 2000.
[17] Wiggenraad J, Michielsen A, Santoro D, Lepage F, Kindervater C, Beltran F, et al. Finite element methodologies development to simulate the behaviour of composite fuselage structure and correlation with drop test. Air Space Europe 2001;3(3-4):228–33. doi:10.1016/S1290-0958(01)90102-9.
[18] Jackson KE, Fasanella EL. Crash Simulation of Vertical Drop Tests of Two Boeing 737 Fuselage sectizns. Tech. Rep.. Army Vehicle Technology Directorate Hampton VA; 2002.
[19] Shoji H, Minegishi M, Aoki T. Impact characteristics estimation of channel section short column under axial impact load. In: 48th AIAA/ASME/ASCE/AHS/ASC structures, structural dynamics, and materials conference; 2007. p. 2023. doi:10.2514/6.2007-2023.
[20] Fasanella EL, Jackson KE, Lyle KH, Sparks CE, Sareen AK. Multi-terrain impact tests and simulations of an energy absorbing fuselage section. J Am Helicopter Soc 2007;52(2):159–68. doi:10.4050/JAHS.52.159.
[21] Ren Y, Xiang J. A comparative study of the crashworthiness of civil aircraft with different strut configurations. Int J Crashworthiness 2010;15(3):321–30. doi:10.1080/13588260903343823.
[22] Zou T, Mou H, Feng Z. Research on effects of oblique struts on crashworthiness of composite fuselage sections. J Aircraft 2012;49(6):2059–63. doi:10.2514/1.C031867.
[23] Jia X, Chen G, Yu Y, Li G, Zhu J, Luo X, et al. Effect of geometric factor, winding angle and pre-crack angle on quasi-static crushing behavior of filament wound CFRP cylinder. Compo Part B 2013;45(1):1336–43. doi:10.1016/j.compositesb.2012.09.060.
[24] Tay YY, Bhonge PS, Lankarani HM. Crash simulations of aircraft fuselage section in water impact and comparison with solid surface impact. Int J Crashworthiness 2015;20(5):464–82. doi:10.1080/13588265.2015.1033972.
[25] Paz J, Díaz J, Romera L, Costas M. Size and shape optimization of aluminum tubes with GFRP honeycomb reinforcements for crashworthy aircraft structures. Compos Struct 2015;133:499–507. doi:10.1016/j.compstruct.2015.07.077.
[26] Ren Y, Xiang J, Zheng J, Luo Z. Crashworthiness analysis of aircraft fuselage with sine-wave beam structure. Chin J Aeronaut 2016;29(2):403–10. doi:10.1016/j.cja.2016.02.002.
[27] Schatrow P, Waimer M. Crash concept for composite transport aircraft using mainly tensile and compressive absorption mechanisms. CEAS Aeronaut J 2016;7(3):471–82.
[28] Paz J, Romera L, Díaz J. Crashworthiness optimization of aircraft hybrid energy absorbers enclosing honeycomb and foam structures. AIAA J 2017;55(2):652–61. doi:10.2514/1.J055245.
[29] Kitazaki S, Griffin MJ. Resonance behaviour of the seated human body and effects of posture. J Biomech 1997;31(2):143–9. doi:10.1016/S0021-9290(97)00126-7.
[30] Mondal P, Arunachalam S. Unique finite element modelling of human body inside accelerating car to predict accelerations and frequencies at different human segments. Appl Sci 2020;10(5):1861. doi:10.3390/app10051861.
[31] Cho Y, Yoon Y-S. Biomechanical model of human on seat with backrest for evaluating ride quality. Int J Ind Ergon 2001;27(5):331–45. doi:10.1016/S0169-8141(00)00061-5.
[32] Wu J, Qiu Y. Modelling of seated human body exposed to combined vertical, lateral and roll vibrations. J Sound Vib 2020;485:115509. doi:10.1016/j.jsv.2020.115509.
[33] Tuned mass damper. Accessed January 2020. URL https://en.wikipedia.org/wiki/Tuned_mass_damper/.
[34] Dimitrijević J, Kovačević P. Computational modal analysis of the Lasta aircraft. Sci Tech Rev 2010;60(1):60–9.
[35] LS-DYNA. LS-DYNA software. Accessed May 2020. URL http://www.lstc.com/.
[36] Dvorkin EN, Goldschmit MB. Nonlinear continua. Springer Science & Business Media; 2006.
[37] LSTC. LS-DYNA R10.0 Keyword Manual Vol. I. Accessed May 2020. http://ftp.lstc.com/anonymous/outgoing/jday/manuals/LS-DYNA_Manual_Volume_I_R10.0.pdf.
[38] Kaniowski J, Wronicz W, Jachimowicz J, Szymczyk E. Methods for FEM analysis of riveted joints of thin-walled aircraft structures within the IMPERJA project. In: ICAF 2009, bridging the gap between theory and operational practice. Springer; 2009. p. 939–67. doi:10.1007/978-90-481-2746-7_52.
[39] LSTC. LS-DYNA Theory Manual, R:9320. 2017. URL http://ftp.lstc.com/anonymous/outgoing/jday/manuals/.
[40] International S.. Instrumentation for impact test-PART 1-Electronic Instrumentation. Accessed February 2020. https://law.resource.org/pub/us/cfr/ibr/005/sae.j211-1.1995.html#:~:text=3.7%20Channel%20Frequency%20Class%2C%20CFC,CFCs%20of%20180%20and%2060.
[41] LS-DYNA dummy modelsAccessed July 2020a;URL https://www.lstc.com/download/dummy_models/.
[42] Mode shapes of 100 LS-DYNA ATD computed by the authorsAccessed May 2020b;URL http://www.asergeev.com/files/lsdyna/movies/2020-05-21/2020-05-21a.htm.
[43] Mode shapes of 40 rubber dummies computed by the authorsAccessed May 2020;URL http://www.asergeev.com/files/lsdyna/movies/2020-05-21/2020-05-21b.htm.
[44] The Charleston dance. Accessed October 2019. URL https://gfycat.com/neglectedhalfaffenpinscher.
[45] Nontrivial mode shapes of 80 eigenmodes showing the coupling motions of the dummies with the aircraft fixture. Accessed June 2020. URL http://www.asergeev.com/files/lsdyna/movies/2020-06-29/index.htm.
[46] Harris Federal Employee Law Firm: Common Types of Injuries. Accessed April 2020. URL https://www.federaldisability.com/legal-services/federal-disability-retirement/injury-types/common-types-injuries/.
[47] IMayo ClinicAccessed August 2020;URL http://www.mayoclinic.org.
[48] Fractal Landscape. Accessed August 2020. URL https://en.wikipedia.org/wiki/Fractal_landscape.
[49] Ebert DS, Musgrave FK, Peachey D, Perlin K, Worley S. Texturing & modeling: a procedural approach. Morgan Kaufmann; 2003.
[50] Chen G, Wang Y-C, Perronnet A, Gu C, Yao P, Bin-Mohsin B, et al. The advanced role of computational mechanics and visualization in science and technology: analysis of the Germanwings Flight 9525 crash. Phys Scr 2017;92(3):033002. doi:10.1088/1402-4896/aa593a.